Publication Year	2020
Acceptance in OA	2025-03-10T10:23:04Z
Title	Angular momentum profiles of Class 0 protostellar envelopes
Authors	Gaudel, M., Maury, A. J., Belloche, A., Maret, S., André, Ph., Hennebelle, P., Galametz, M., TESTI, Leonardo, Cabrit, S., Palmeirim, P., Ladjelate, B., CODELLA, Claudio, PODIO, Linda
Publisher's version (DOI)	10.1051/0004-6361/201936364
Handle	http://hdl.handle.net/20.500.12386/36563
Journal	ASTRONOMY & ASTROPHYSICS
Volume	637

A&A 637, A92 (2020)
https://doi.org/10.1051/0004-6361/201936364

Astronomy & Astrophysics

Angular momentum profiles of Class 0 protostellar envelopes[⋆]

M. Gaudel[1,2,3], A. J. Maury[1,4], A. Belloche[2], S. Maret[5], Ph. André[1], P. Hennebelle[1], M. Galametz[1], L. Testi[6], S. Cabrit[3], P. Palmeirim[7], B. Ladjelate[8], C. Codella[9], and L. Podio[9]

[1] Laboratoire AIM, CEA Saclay/DRF/IRFU, CNRS, Université Paris-Saclay, Université Paris Diderot, Sorbonne Paris Cité, 91191 Gif-sur-Yvette, France
e-mail: `mathilde.gaudel@obspm.fr`
[2] Max-Planck-Institut für Radioastronomie, Auf dem Hügel 69, 53121 Bonn, Germany
[3] LERMA, Observatoire de Paris, PSL Research University, CNRS, Sorbonne Université, UPMC Université Paris 06, 75014 Paris, France
[4] Harvard-Smithsonian Center for Astrophysics, Cambridge, MA, USA
[5] Univ. Grenoble Alpes, CNRS, IPAG, 38000 Grenoble, France
[6] ESO, Karl Schwarzschild Strasse 2, 85748 Garching bei München, Germany
[7] Instituto de Astrofísica e Ciências do Espaço, Universidade do Porto, CAUP, Rua das Estrelas, 4150-762 Porto, Portugal
[8] Instituto Radioastronomia Milimétrica, Av. Divina Pastora 7, Nucleo Central, 18012 Granada, Spain
[9] INAF – Osservatorio Astrofisico di Arcetri, Largo E. Fermi 5, 50125 Firenze, Italy

Received 23 July 2019 / Accepted 24 January 2020

ABSTRACT

Context. Understanding the initial properties of star forming material and how they affect the star formation process is a key question. The infalling gas must redistribute most of its initial angular momentum inherited from prestellar cores before reaching the central stellar embryo. Disk formation has been naturally considered as a possible solution to this "angular momentum problem". However, how the initial angular momentum of protostellar cores is distributed and evolves during the main accretion phase and the beginning of disk formation has largely remained unconstrained up to now.

Aims. In the framework of the IRAM CALYPSO survey, we obtained observations of the dense gas kinematics that we used to quantify the amount and distribution of specific angular momentum at all scales in collapsing-rotating Class 0 protostellar envelopes.

Methods. We used the high dynamic range $C^{18}O$ (2−1) and N_2H^+ (1−0) datasets to produce centroid velocity maps and probe the rotational motions in the sample of 12 envelopes from scales ~50 to ~5000 au.

Results. We identify differential rotation motions at scales $\lesssim$1600 au in 11 out of the 12 protostellar envelopes of our sample by measuring the velocity gradient along the equatorial axis, which we fit with a power-law model $v \propto r^{\alpha}$. This suggests that coherent motions dominate the kinematics in the inner protostellar envelopes. The radial distributions of specific angular momentum in the CALYPSO sample suggest the following two distinct regimes within protostellar envelopes: the specific angular momentum decreases as $j \propto r^{1.6\pm0.2}$ down to ~1600 au and then tends to become relatively constant around $\sim 6 \times 10^{-4}$ km s^{-1} pc down to ~50 au.

Conclusions. The values of specific angular momentum measured in the inner Class 0 envelopes suggest that material directly involved in the star formation process (<1600 au) has a specific angular momentum on the same order of magnitude as what is inferred in small T-Tauri disks. Thus, disk formation appears to be a direct consequence of angular momentum conservation during the collapse. Our analysis reveals a dispersion of the directions of velocity gradients at envelope scales >1600 au, suggesting that these gradients may not be directly related to rotational motions of the envelopes. We conclude that the specific angular momentum observed at these scales could find its origin in other mechanisms, such as core-forming motions (infall, turbulence), or trace an imprint of the initial conditions for the formation of protostellar cores.

Key words. stars: formation – stars: protostars – ISM: kinematics and dynamics – radio lines: ISM

1. Introduction

Stars form via the gravitational collapse of $\lesssim$0.1 pc dense cores, which are embedded within molecular clouds (André et al. 2000; Ward-Thompson et al. 2007; di Francesco et al. 2007). Prestellar cores become unstable and collapse due to their own gravitational potential. One or several stellar embryos form in their center. This is the beginning of the main accretion phase called the protostellar phase. Observations of the molecular line emission from large samples of cores in close star-forming regions revealed that velocity gradients are ubiquitous to prestellar structures at scales of 0.1−0.5 pc (Goodman et al. 1993; Caselli et al. 2002). These were interpreted as slow rotation inherited from their formation process (Goodman et al. 1993; Caselli et al. 2002; Ohashi et al. 1999; Redman et al. 2004; Williams et al. 2006). Assuming these gradients trace organized rotational motions, the observed velocities lead to a typical angular rotation velocity of $\Omega \sim 2$ km s^{-1} pc^{-1} and specific angular momentum values of $j = v \times r \sim 10^{-3}$–$10^{-1}$ km s^{-1} pc.

During the collapse, if the angular momentum of the parent prestellar cores is totally transferred to the stellar embryo, the gravitational force can not counteract the centrifugal force and the stellar embryo fragments prematurely before reaching the main sequence. This is the angular momentum problem for star formation (Bodenheimer 1995). Although observational studies suggest a trend of decreasing specific angular momentum toward

---

[⋆] The datasets used in this paper are available at `http://www.iram.fr/ILPA/LP010/`

smaller core sizes of $j \propto r^{1.6}$, the j measured in prestellar structures at scales of 10 000 au ($\sim 10^{-3}$ km s^{-1} pc, Caselli et al. 2002) is still typically three orders of magnitude higher than the one associated with the maximum rotational energy that a solar-type star can sustain ($j_{\rm break} \sim 10^{18}$ cm^2 s^{-1} $\sim 3 \times 10^{-6}$ km s^{-1} pc). The physical mechanisms responsible for the angular momentum redistribution before the matter is accreted by the central stellar object have still to be identified.

During the star formation process, disk formation is expected to be a consequence of angular momentum conservation during the collapse of rotating cores (Cassen & Moosman 1981; Terebey et al. 1984). From observational studies, disks are common in Class II objects (Andrews et al. 2009; Isella et al. 2009; Ricci et al. 2010; Spezzi et al. 2013; Piétu et al. 2014; Cieza et al. 2019). Thus, disk formation has been naturally considered as a possible solution to the angular momentum problem by redistributing the four orders of magnitude of j measured from prestellar cores to the T-Tauri stars ($j \sim 2 \times 10^{-7}$ km s^{-1} pc, Bouvier et al. 1993): the disk would store and evacuate the angular momentum of the matter by viscous friction (Lynden-Bell & Pringle 1974; Hartmann et al. 1998; Najita & Bergin 2018) or thanks to disk winds (Blandford & Payne 1982; Pelletier & Pudritz 1992; Pudritz et al. 2007) before the matter is accreted by the central stellar object. However, the spatial distribution of angular momentum during disk formation within star-forming structures at scales between the outer core radius and the stellar surface are still largely unconstrained.

Class 0 protostars are the first (proto)stellar objects observed after the collapse in prestellar cores (André et al. 1993, 2000). Due to their youth, most of their mass is still in the form of a dense, collapsing, reservoir envelope surrounding the central stellar embryo ($M_{\rm env} \gg M_\star$). Thus, they are likely to retain the initial conditions inherited from prestellar cores, in particular regarding angular momentum. The young stellar embryo mass increases via the accretion of the gaseous and dusty envelope in a short timescale ($t < 10^5$ yr, Evans et al. 2009; Maury et al. 2011). During this main accretion phase, most of the final stellar mass is accreted and, at the same time, the infalling gas must redistribute most of its initial angular momentum before reaching the central stellar embryo. Class 0 protostars are therefore key objects to understand the distribution of angular momentum of the material directly involved in the star formation process and constrain physical mechanisms responsible for the redistribution as disk formation.

Clear signatures of rotation (Belloche et al. 2002; Belloche & André 2004; Chen et al. 2007) and infalling gas are generally detected in the envelopes of Class 0 protostars (see the review by Ward-Thompson et al. 2007). Thanks to observations of the dense molecular gas emission, rotational motions where characterized in seven Class 0 or I protostellar envelopes at scales between 3500 and 10000 au (Ohashi et al. 1997a; Belloche et al. 2002; Chen et al. 2007). These envelopes exhibit an average angular momentum of $\sim 10^{-3}$ km s^{-1} pc at scales of $r < 5000$ au, consistent with the j measured in prestellar cores by Caselli et al. (2002) ($\sim 10^{-3}$ km s^{-1} pc). These studies suggest an angular momentum that is constant with radius in Class 0 protostellar envelopes. These flat profiles are generally interpreted as the conservation of the angular momentum. From hydrodynamical simulations, the conservation of these typical values of angular momentum results in the formation of large rotationally supported disks with radii >100 au in a few thousand years (Yorke & Bodenheimer 1999). However, from observational studies, large disks are rare around Class 0 protostars ($r < 100$ au, Maury et al. 2010, 2019; Kurono et al. 2013; Yen et al. 2013; Segura-Cox et al. 2016). Only recent numerical simulations including magnetohydrodynamics and non-ideal effects, such as ambipolar diffusion, Ohmic dissipation, or the Hall effect, allow small rotationally supported disks to be formed (< 100 au; Machida et al. 2014; Tsukamoto et al. 2015; Masson et al. 2016).

Very few studies have been able to produce resolved profiles of angular momentum to characterize the actual amount of angular momentum present at the smallest scales ($r \lesssim 1000$ au) within protostellar envelopes. From interferometric observations, Yen et al. (2015a) derive specific angular momentum values of $\sim 2 \times 10^{-4}$ km s^{-1} pc in seven Class 0 envelopes at scales of $r \sim 1000$ au, values which are below the trend observed by Ohashi et al. (1997a). These studies have put constraints on the angular momentum properties of Class 0 protostellar envelopes and suggest the material at $r \sim 1000$ au must reduce its angular momentum by at least one order of magnitude from outer envelope to disk scales. Yen et al. (2011, 2017) show specific angular momentum profiles down to ∼350 au in two Class 0 protostellar envelopes: $j \sim 6 \times 10^{-4}$ km s^{-1} pc at $r \sim 1000$ au and $j \lesssim 10^{-4}$ km s^{-1} pc at $r \sim 350$ au. In this case, conservation of angular momentum during rotating protostellar collapse might not be the dominant process leading to the formation of disks and stellar multiple systems. It is therefore crucial to obtain robust estimates of the angular momentum of the infalling material in protostellar envelopes during the main accretion phase by analyzing the kinematics from the outer regions of the envelope (10 000 au, Motte & André 2001) to the protostellar disk (<50 au, Maury et al. 2019).

2. The CALYPSO survey

The Continuum And Lines in Young ProtoStellar Objects (CALYPSO[1]) IRAM Large Program is a survey of 16 nearby Class 0 protostars ($d < 450$ pc), carried out with the IRAM Plateau de Bure interferometer (PdBI) and IRAM 30-meter telescope (30m) at wavelengths of 1.29, 1.37, and 3.18 mm. The CALYPSO sources are among the youngest known solar-type Class 0 objects (André et al. 2000) with envelope masses of $M_{\rm env} \sim 1.5\ M_\odot$ and internal luminosities of $L_{\rm bol} \sim 0.1{-}30\ L_\odot$ (Maury et al. 2019).

The CALYPSO program allows us to study in detail the Class 0 envelope chemistry (Maury et al. 2014; Anderl et al. 2016; De Simone et al. 2017; Belloche et al. 2020), disk properties (Maret et al. 2014, 2020; Maury et al. 2019) and protostellar jets (Codella et al. 2014a; Santangelo et al. 2015; Podio et al. 2016, and in prep.; Lefèvre et al. 2017; Anderl et al. 2020). One of the main goals of this large observing program is to understand how the circumstellar envelope is accreted onto the central protostellar object during the Class 0 phase, and ultimately tackle the angular momentum problem of star formation. This paper presents an analysis of envelope kinematics, for the 12 sources from the CALYPSO sample located at $d \leq 350$ pc (see Table 1) and discuss our results on the properties of the angular momentum in Class 0 protostellar envelopes.

We adopt the dust continuum peak at 1.3 mm (225 GHz) determined from the PdBI datasets by Maury et al. (2019) as origin of the coordinate offsets of the protostellar envelopes (see Table 1). We report for each source in Table 1 the outflow axis considered as the rotation axis and estimated by

---

[1] See `http://irfu.cea.fr/Projets/Calypso/` and `http://www.iram-institute.org/EN/content-page-317-7-158-240-317-0.html`

Table 1. Sample of CALYPSO Class 0 protostars considered for this analysis.

Source $^{(a)}$	RA (J2000) (h:m:s)	Dec (J2000) $^{(b)}$ (°:′:″)	$d^{(c)}$ (pc)	$L_{\rm int}{}^{(d)}$ ($L_{\odot}$)	$M_{\rm env}{}^{(e)}$ ($M_{\odot}$)	$R_{\rm env}{}^{(f)}$ (au)	PA outflow $^{(g)}$ (°)	$i^{(h)}$ (°)	Refs $^{(i)}$
L1448-2A1 L1448-2A2	03:25:22.405 03:25:22.355	30:45:13.26 30:45:13.16	293	4.7	1.9	5300	-63 (blue), +140 (red)$^{(\star)}$	30 ± 10	1, 2, 3, 4
L1448-NB1 L1448-NB2	03:25:36.378 03:25:36.315	30:45:14.77 30:45:15.15	293	3.9	4.8	9700	−80	30 ± 15	5, 6, 7, 4-8
L1448-C	03:25:38.875	30:44:05.33	293	10.9	2.0	7300	−17	20 ± 5	9, 6, 7, 10-11
IRAS2A	03:28:55.570	31:14:37.07	293	47	7.9	10000	+205	30 ± 15	12, 13, 7, 14-15
SVS13-B	03:29:03.078	31:15:51.74	293	3.1	2.8	2100	+167	30 ± 20$^{(\star\star)}$	16, 17, 3, ...
IRAS4A1 IRAS4A2	03:29:10.537 03:29:10.432	31:13:30.98 31:13:32.12	293	4.7	12.3	1700	+180	15 ± 10	12, 6, 3, 18
IRAS4B	03:29:12.016	31:13:08.02	293	2.3	4.7	3200	+167	20 ± 15	12, 6, 7, 19
IRAM04191	04:21:56.899	15:29:46.11	140	0.05	0.5	14000	+20	40 ± 10	20, 21, 7, 22
L1521F	04:28:38.941	26:51:35.14	140	0.035	0.7−2	4500	+240	20 ± 20	23, 24, 3, 25
L1527	04:39:53.875	26:03:09.66	140	0.9	1.2	17000	+90	3 ± 5	26, 7, 7, 25
L1157	20:39:06.269	68:02:15.70	352	4.0	3.0	15800	+163	10 ± 10	27, 7, 7, 28-29
GF9-2	20:51:29.823	60:18:38.44	200	0.3	0.5	7000	0	30 ± 20$^{(\star\star)}$	30, 31, 3, ...

Notes. $^{(a)}$Name of the protostars with the multiple components resolved by the 1.3 mm continuum emission from PdBI observations (Maury et al. 2019). $^{(b)}$Coordinates of the continuum emission peak at 1.3 mm from Maury et al. (2019). $^{(c)}$Distance assumed for the individual sources. We adopt a value of 140 pc for the Taurus distance estimated from a VLBA measurement (Torres et al. 2009). The distances of Perseus and Cepheus are taken following recent *Gaia* parallax measurements that have determined a distance of (293 ± 20) pc (Ortiz-León et al. 2018) and (352 ± 18) pc (Zucker et al. 2019), respectively. We adopt a value of 200 pc for the GF9-2 cloud distance (Wiesemeyer 1997; Wiesemeyer et al. 1998) but this distance is very uncertain and some studies estimated a higher distance between 440–470 pc (Viotti 1969, C. Zucker, priv. comm.) and 900 pc (Reid et al. 2016). $^{(d)}$Internal luminosities which come from the analysis of *Herschel* maps from the Gould Belt survey (HGBS, André et al. 2010 and Ladjelate et al., in prep.) and corrected by the assumed distance. $^{(e)}$Envelope mass corrected by the assumed distance. $^{(f)}$Outer radius of the individual protostellar envelope determined from dust continuum emission, corrected by the assumed distance. We adopt the radius from PdBI dust continuum emission (Maury et al. 2019) when we do not have any information on the 30m continuum from Motte & André (2001) and for IRAS4A which is known to be embedded into a compressing cloud (Belloche et al. 2006). $^{(g)}$Position angle of the blue lobe of the outflows estimated from CALYPSO PdBI ^{12}CO and SiO emission maps (Podio & CALYPSO, in prep.). PA is defined east from north. Sources indicated with $^{(\star)}$ have an asymmetric outflow and the position angles of both lobes are reported. For IRAS2A, IRAS4A, and L1157, previous works done by Codella et al. (2014b), Santangelo et al. (2015), and Podio et al. (2016), respectively, show a detailed CALYPSO view of the jets. For L1521F, we use the PA estimated by Tokuda et al. (2014, 2016). $^{(h)}$Inclination angle of the equatorial plane with respect to the line of sight. Sources indicated with $^{(\star\star)}$have an inclination angle not well constrained, so we assumed a default value of (30 ± 20)°. $^{(i)}$References for the protostar discovery paper, the envelope mass, the envelope radius and then the inclination are reported here.

References. (1) O'Linger et al. (1999); (2) Enoch et al. (2009); (3) Maury et al. (2019); (4) Tobin et al. (2007); (5) Curiel et al. (1990); (6) Sadavoy et al. (2014); (7) Motte & André (2001); (8) Kwon et al. (2006); (9) Anglada et al. (1989); (10) Bachiller et al. (1995); (11) Girart & Acord (2001); (12) Jennings et al. (1987); (13) Karska et al. (2013); (14) Codella et al. (2004); (15) Maret et al. (2014); (16) Grossman et al. (1987); (17) Chini et al. (1997); (18) Ching et al. (2016); (19) Desmurs et al. (2009); (20) André et al. (1999); (21) André et al. (2000); (22) Belloche et al. (2002); (23) Mizuno et al. (1994); (24) Tokuda et al. (2016); (25) Terebey et al. (2009); (26) Ladd et al. (1991); (27) Umemoto et al. (1992); (28) Gueth et al. (1996); (29) Bachiller et al. (2001); (30) Schneider & Elmegreen (1979); (31) Wiesemeyer (1997).

Podio & CALYPSO (in prep.) from high-velocity emission of ^{12}CO, SiO, and SO at scales <10″. We assume the equatorial axis of the protostellar envelopes, namely the intersection of the equatorial plane with the plane of the sky at the distance of the source, to be perpendicular to the rotation axis. The SiO emission in the CALYPSO maps is very collimated, so the uncertainties on the direction of the rotation axis, and thus on the direction of the equatorial axis, are smaller than ±10° (Podio & CALYPSO, in prep.). For L1521-F, IRAM04191, and GF9-2, no collimated SiO jet is detected, thus, the uncertainties are a bit larger (±20°). We also use estimates of the inclination of the equatorial plane with respect to the line of sight from the literature. These estimates, which come from geometric models that best reproduce the outflow kinematics observed in molecular emission, are highly uncertain since we do not have access to the 3D-structure of each source.

3. Observations and dataset reduction

To probe the dense gas in our sample of protostellar envelopes, we use high spectral resolution observations of the emission of two molecular lines, $C^{18}O$ (2−1) at 219.560 GHz and N_2H^+ (1−0) at 93.171 GHz. In this section, we describe the dataset properties exploited to characterize the kinematics of the envelopes at radii between r ~50 and 5000 au from the central object.

3.1. Observations with the IRAM Plateau de Bure Interferometer

Observations of the 12 protostellar envelopes considered here were carried out with the IRAM Plateau de Bure Interferometer (PdBI) between September 2010 and March 2013. We used the

6-antenna array in two configurations (A and C), providing baselines ranging from 16 to 760 m, to carry out observations of the dust continuum emission and a dozen molecular lines, using three spectral setups (around 94, 219, and 231 GHz). Gain and flux were calibrated using CLIC which is part of the GILDAS[2] software. The details of CALYPSO observations and the calibration carried out are presented in Maury et al. (2019). The phase self-calibration corrections derived from the continuum emission gain curves, described in Maury et al. (2019), were also applied to the line visibility dataset (for all sources in the restricted sample studied here except the faintest sources IRAM04191, L1521F, GF9-2, and L1448-2A). Here, we focus on the $C^{18}O$ (2−1) emission line at 219 560.3190 MHz and the N_2H^+ (1−0) emission line at 93 176.2595 MHz, observed with high spectral resolution (39 kHz channels, i.e., a spectral resolution of 0.05 km s^{-1} at 1.3 mm and 0.13 km s^{-1} at 3 mm). The $C^{18}O$ (2−1) maps were produced from the continuum-subtracted visibility tables using either (i) a robust weighting of 1 for the brightest sources to minimize the side-lobes, or (ii) a natural weighting for the faintest sources (IRAM04191, L1521F, GF9-2, and L1448-2A) to minimize the rms noise values. We resampled the spectral resolution to 0.2 km s^{-1} to improve the signal-to-noise ratio (S/N) of compact emission. The N_2H^+ (1−0) maps were produced from the continuum-subtracted visibility tables using a natural weighting for all sources. In all cases, deconvolution was carried out using the Hogbom algorithm in the MAPPING program of the GILDAS software.

3.2. Short-spacing observations from the IRAM 30-m telescope

The short-spacing observations were obtained at the IRAM 30-m telescope (30m) between November 2011 and November 2014. Details of the observations for each source are reported in Table A.1. We observed the $C^{18}O$ (2−1) and N_2H^+ (1−0) lines using the heterodyne Eight MIxer Receiver (EMIR) in two atmospheric windows: E230 band at 1.3 mm and E090 band at 3 mm (Carter et al. 2012). The Fast Fourier Transform Spectrometer (FTS) and the VErsatile SPectrometer Array (VESPA) were connected to the EMIR receiver in both cases. The FTS200 backend provided a large bandwidth (4 GHz) with a spectral resolution of 200 kHz (0.27 km s^{-1}) for the $C^{18}O$ line, while VESPA provided high spectral resolution observations (20 kHz channel or 0.063 km s^{-1}) of the N_2H^+ line. We used the on-the-fly spectral line mapping, with the telescope beam moving at a constant angular velocity to sample regularly the region of interest ($1' \times 1'$ coverage for the $C^{18}O$ emission and $2' \times 2'$ coverage for the N_2H^+ emission). The mean atmospheric opacity at 225 GHz was $\tau_{225} \sim 0.2$ during the observations at 1.3 mm and $\tau_{225} \sim 0.5$ during the observations at 3 mm. The mean values of atmospheric opacity are reported for each source in Table A.1. The telescope pointing was checked every 2−3 h on quasars close to the CALYPSO sources, and the telescope focus was corrected every 4−5 h using the planets available in the sky. The single-dish dataset were reduced using the MIRA and CLASS programs of the GILDAS software following the standard steps: flagging of incorrect channels, temperature calibration, baseline subtraction, and gridding of individual spectra to produce regularly-sampled maps.

3.3. Combination of the PdBI and 30m data

The IRAM PdBI observations are mostly sensitive to compact emission from the inner envelope. Inversely, single-dish dataset contains information at envelope scales ($r \sim 5{-}40''$) but its angular resolution does not allow us to characterize the inner envelope emission at scales smaller than the beamwidth. To constrain the kinematics at all relevant scales of the envelope, one has to build high angular resolution dataset which recovers all emission of protostellar envelopes. We merged the PdBI and the 30m datasets (hereafter PdBI + 30m) for each tracer using the pseudo-visibility method[3]: we generated pseudo-visibilities from the Fourier transformed 30m image data, which are then merged to the PdBI dataset in the MAPPING program of the GILDAS software. This process degrades the angular resolution of the PdBI dataset but recovers a large fraction of the extended emission. The spectral resolution of the combined PdBI + 30m dataset is limited by the 30m dataset at 1.3 mm (0.27 km s^{-1}) and the PdBI one at 3 mm (0.13 km s^{-1}).

We produced the N_2H^+ (1−0) combined datacubes in such a way to have a synthesized beam size $<2''$ and a noise level <10 mJy $beam^{-1}$. As the N_2H^+ emission traces preferably the outer protostellar envelope, we used a natural weighting to build the combined maps to minimize the noise rather than to maximize angular resolution. The $C^{18}O$ (2−1) combined maps were produced using a robust weighting scheme, in order to obtain synthesized beam sizes close to the PdBI ones, and to minimize the side-lobes. In all cases, the deconvolution was carried out using the Hogbom algorithm in MAPPING.

3.4. Properties of the analyzed maps

Following the procedure described above, we have obtained, for each source of the sample, a set of three cubes for each of the two molecular tracers $C^{18}O$ (2−1) and N_2H^+ (1−0), probing the emission at different spatial scales (PdBI map, combined PdBI+30m map, and 30m map). In order to build maps with pixels that contain independent dataset and avoid oversampling, we inversed visibilities from the PdBI and the combined PdBI+30m datasets using only 4 pixels per synthesized beam, and we smoothed the resulting maps afterwards to obtain 2 pixels per element of resolution. The properties of the resulting maps are reported in Appendix B. The spatial resolution of the molecular line emission maps is reported in Tables B.1 and B.2. The spatial extent of the molecular emission, the rms noise levels, and the integrated fluxes are reported in Tables B.3 and B.4.

4. Envelope kinematics from high dynamic range datasets

4.1. Integrated intensity maps

To identify at which scales of the protostellar envelopes the different datasets are sensitive to, we produced integrated intensity maps by integrating spectra of each pixel for the molecular lines $C^{18}O$ (2−1) and N_2H^+ (1−0) from the PdBI, combined, and 30m datasets for each source. For $C^{18}O$ (2−1), we integrated each spectrum on a velocity range of ± 2.5 km s^{-1} around the velocity of the peak of the mean spectrum of each source. The 1−0 line of N_2H^+ has a hyperfine structure with seven components (see Fig. 2). We integrated the N_2H^+ spectra over a range

---

[2] See `http://www.iram.fr/IRAMFR/GILDAS/` for more information about the GILDAS software (Pety 2005).

[3] For details, see `http://www.iram.fr/IRAMFR/GILDAS/doc/pdf/map.pdf`

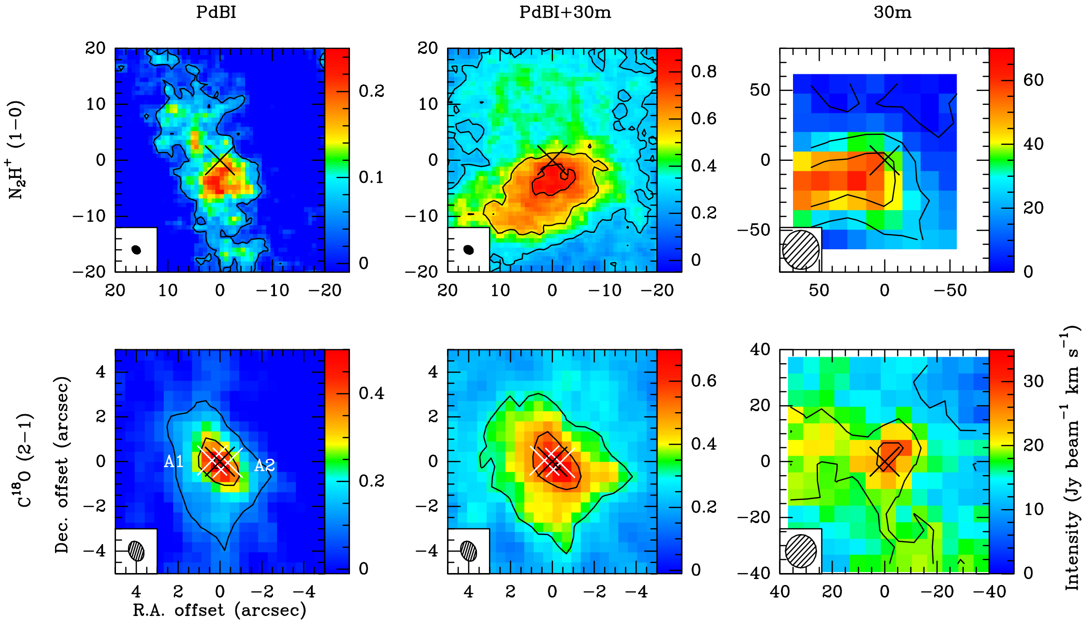

Fig. 1. Integrated intensity maps of N_2H^+ (1−0) (*top*) and $C^{18}O$ (2−1) (*bottom*) emission from the PdBI (*left*), combined (*middle*), and 30m (*right*) datasets for L1448-2A. The white crosses represent the positions of the binary system determined from the 1.3 mm dust continuum emission. The black cross represents the middle position between the binary system. The clean beam is shown by an ellipse on the bottom left of each map. The black lines represent the integrated intensity contours of each tracer starting at 5σ and increasing in steps of 25σ for N_2H^+ and 10σ for $C^{18}O$ (see Tables B.3 and B.4). Be careful, the spatial scales of the maps are not uniform in all panels.

of 20 km s^{-1} encompassing the seven components. Figure 1 shows as an example the integrated intensity maps obtained for L1448-2A. The integrated intensity maps of the other sources are provided in Appendix H.

We used the integrated intensity maps to measure the average emission size of each tracer in each dataset above a 5σ threshold. The values reported in Tables B.3 and B.4 are the average of two measurements: an intensity cut along the equatorial axis and circular averages at different radii around the intensity peak position of the source. Only pixels whose intensity is at least 5 times higher than the noise in the map are considered to build these intensity profiles. The FWHM of the adjustment by a Gaussian function allows us to determine the average emission size of the sources. For both tracers and for all sources in our sample, the emission is detected above 5σ in an area larger in the combined datasets than in the PdBI datasets, and smaller than in the 30m ones (see Tables B.3 and B.4). Our three datasets are thus not sensitive to the same scales and allow us to probe different scales within the 12 sampled protostellar envelopes: the 30m datasets trace the outer envelope, the PdBI datasets the inner part and the combined ones the intermediate scales.

The $C^{18}O$ and N_2H^+ molecules do not trace the same regions of the protostellar envelope either: Anderl et al. (2016) report from an analysis of the CALYPSO survey that the N_2H^+ emission forms a ring around the central C18O emission in four sources. Previous studies (Bergin et al. 2002; Maret et al. 2002, 2007; Anderl et al. 2016) show that N_2H^+, which is abundant in the outer envelope, is chemically destroyed when the temperature in the envelope reaches the critical temperature ($T \gtrsim 20$K) at which CO desorbs from dust ice mantles. Thus, while N_2H^+ can be used to probe the envelope kinematics at outer envelope scales, $C^{18}O$ can be used as a complementary tracer of the gas kinematics at smaller radii where the embedded protostellar embryo heats the gas to higher temperatures.

The $C^{18}O$ emission is robustly detected ($>5\sigma$) in our PdBI observations for most sources, except for L1521F and IRAM04191 which are the lowest luminosity sources of our sample (see Table 1), and for SVS13-B where the emission is dominated by its companion, the Class I protostar SVS13-A. For most sources, the interferometric map obtained with the PdBI shows mostly compact emission ($r < 3''$, see Table B.3). However, the $C^{18}O$ emission from the 30m datasets shows more complex structures (see Appendix H). Assuming that, under the hypothesis of spherical geometry, the emission from a protostellar envelope is compact ($r \lesssim 40''$, i.e., $\lesssim$10000 au, see Table 1) and stands out from the environment in which it is embedded, the 30m emission of L1448-2A, L1448-C, and IRAS4A comes mainly from the envelope.

The N_2H^+ emission is detected in our combined observations for all sources. In the four sources studied by Anderl et al. (2016), they do not detect the emission at the 1.3 mm continuum peak, but emission rings around the $C^{18}O$ central emission. From Table B.4, we noticed two types of emission morphologies based on the PdBI dataset: compact ($r < 7''$, see Table B.4) or filamentary ($r \geq 9''$). In the same way as the $C^{18}O$ emission, the N_2H^+ emission from the 30m datasets shows complex structures with radius $r \gtrsim 40''$ for most sources, except for five sources (IRAM04191, L1521F, L1448-NB, L1448-C, and L1157) where the emission is consistent with the compact emission of the protostellar envelope.

The $C^{18}O$ emission from the PdBI is not centered on the continuum peak for three sources in our sample: IRAS4A, L1448-NB, and L1448-2A (see Appendix H). For each of these sources, the PdBI 1.3 mm dust continuum emission map resolves a close binary system (<600 au) with both components embedded in the same protostellar envelope (Maury et al. 2019, see Table 1). The origin of the coordinate offsets is chosen to be the main protostar, secondary protostar, and the middle of the binary

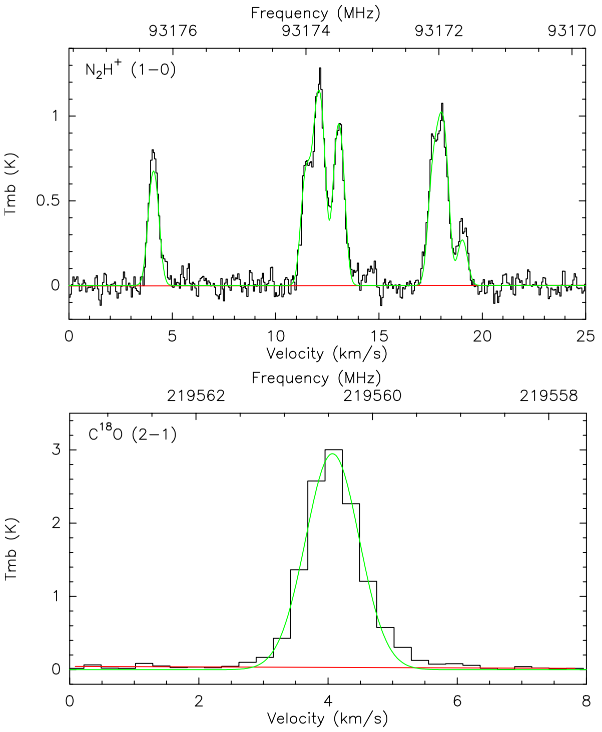

Fig. 2. Mean spectra of the N_2H^+ (*top*) and $C^{18}O$ (*bottom*) molecular lines from the 30m datasets for L1448-2A. The best fits of the spectra, by a hyperfine structure and a Gaussian line profile models respectively, are represented in green solid lines. *Top panel*: the velocity axis corresponds to the isolated HFS component $1_{01} - 0_{12}$. The systemic velocity is estimated to be 4.10 km s^{-1} for this source (see Table E.1).

system for IRAS4A, L1448-NB, and L1448-2A, respectively, to study the kinematics in a symmetrical way.

4.2. Velocity gradients in protostellar envelopes

To quantify centroid velocity variations at all scales of the protostellar envelopes, we produced centroid velocity maps of each Class 0 protostellar envelope by fitting all individual spectra (pixel by pixel) by line profile models in the CLASS program of the GILDAS software. We only considered the line intensity detected with a S/N higher than 5. We fit the spectra to be able to deal with multiple velocity components. Indeed, because protostellar envelopes are embedded in large-scale clouds, multiple velocity components can be expected on some lines of sight where both the protostellar envelope and the cloud emit. For example, Belloche et al. (2006) find several velocity components in their 30m of the N_2H^+ emission of IRAS4A (see Appendix H.6). Except for IRAS4A and IRAS4B for which we fit two velocity components (see details in Appendix H), for most sources we used a Gaussian line profile to model the $C^{18}O$ (2−1) emission, with the line intensity, full width at half maximum (FWHM), and centroid velocity let as free parameters (see Fig. 2). In the case of N_2H^+ (1−0), we used a hyperfine structure (HFS) line profile to determine the FWHM and centroid velocity of the molecular line emission (see Fig. 2). Figures 3–14 show the centroid velocity maps obtained for each source of the sample using the PdBI, combined, and 30m datasets for both the $C^{18}O$ and N_2H^+ emission.

For most sources in our sample, these centroid velocity maps reveal organized velocity patterns with blue-shifted and red-shifted velocity components on both sides of the central stellar embryo, along the equatorial axis where such velocity gradients could be due to rotation of the envelopes. The global kinematics in Class 0 envelopes is a complex combination of rotation, infall, and outflow motions. The observed velocities are projected on the line of sight and thus, are a mix of the various gas motions. Therefore, it is not straightforward to interpret a velocity gradient in terms of the underlying physical process producing it. In order to have an indication of the origin of these gradients, we performed a least-square minimization of a linear velocity gradient model on the velocity maps following:

$$v_{\rm grad} = v_0 + a\Delta\alpha + b\Delta\beta, \tag{1}$$

with $\Delta\alpha$ and $\Delta\beta$ the offsets with respect to the central source (Goodman et al. 1993).

This simple model provides an estimate of the reference velocity v_0 called systemic velocity, the direction Θ, and the amplitude G of the mean velocity gradient. One would expect a mean gradient perpendicular to the outflow axis if the velocity gradient was due to rotational motions in an axisymmetric envelope. A mean gradient oriented along the outflow axis could be due to jets and outflows or infall in a flattened geometry. The gradients were fit on the region of the velocity maps shown in Fig. 3, namely 10″× 10″ in the PdBI and combined datasets for the $C^{18}O$ emission (lower left and central panels), 40″× 40″ for the N_2H^+ emission from the PdBI and combined datasets (upper left and central panels), and 80″× 80″ and 160″× 160″, respectively for the $C^{18}O$ and N_2H^+ emission from the 30m datasets (right panels). Table 2 reports for each source the significant mean velocity gradients detected with an amplitude higher than 2σ. No significant velocity gradient is observed for IRAM04191, L1521F, and SVS13-B in $C^{18}O$ emission at scales of $r < 5''$or for L1448-C and IRAS4B at $r > 30''$(see Table 2).

Seven of the 12 sources in our sample show a mean gradient in $C^{18}O$ emission aligned with the equatorial axis ($\Delta\Theta < 30°$) which could trace rotational motions of the envelope at scales of $r < 5''$. At similar scales, four sources (L1448-NB, L1521F, L1157, GF9-2) show gradients with intermediate orientation ($30° < \Delta\Theta < 60°$). Finally, L1448-2A shows a mean gradient aligned to the outflow axis rather than the equatorial axis ($\Delta\Theta > 60°$). For these last five sources, the gradients observed could be due to a combination of rotation, ejection, and infall motions. For all sources, we noticed a systematic dispersion of the direction of the velocity gradient from inner to outer scales in the envelope (see Fig. 19). We discuss in Sect. 5.4 whether this shift in direction of the velocity gradient is due to a transition from rotation-dominated inner envelope to collapse-dominated outer envelope at $r > 1500$ au, or is due to the different molecular tracers used for this analysis. In most sources, the gradient moves away from the equatorial axis as the scale increases. Only three sources (IRAM04191, L1521F, and L1527) show a gradient close to the equatorial axis with $\Delta\Theta < 30°$ at 2000 au in N_2H^+ emission from the combined dataset while four sources show a complex gradient and five sources have a $\Delta\Theta > 60°$.

4.3. High dynamic range position-velocity diagrams to probe rotational motions

To investigate rotational motions and characterize the angular momentum properties in our sample of Class 0 protostellar envelopes, we build the position-velocity ($PV_{\rm rot}$) diagrams along the equatorial axis. We assumed the position angle of the equatorial axis as orthogonal to the jet axis reported in Table 1. The choice of this equatorial axis allows us to maximize sensitivity

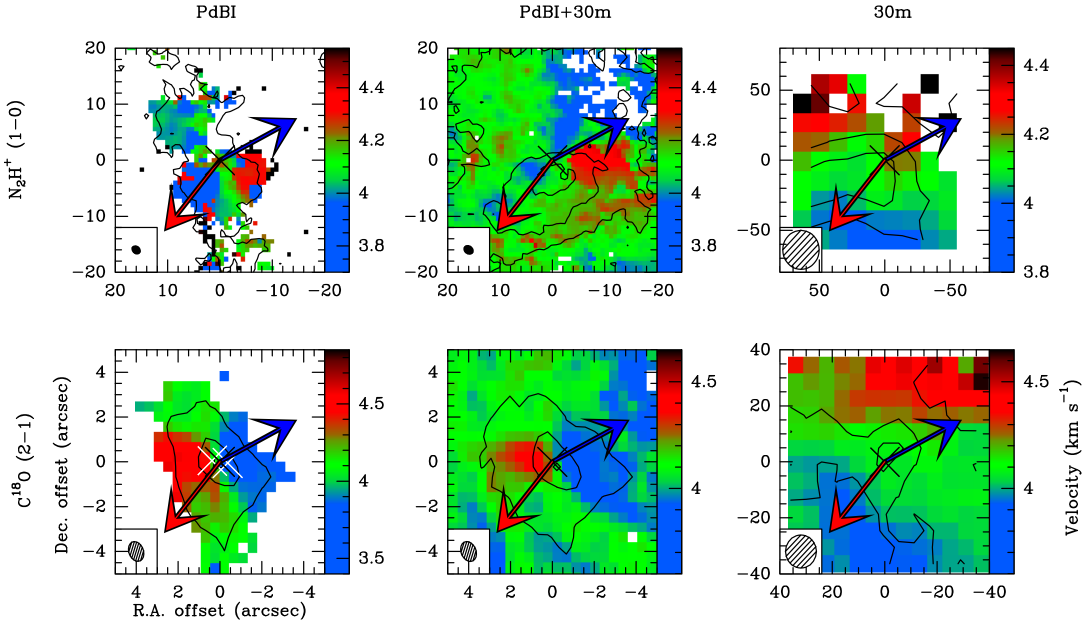

Fig. 3. Centroid velocity maps of N$_2$H$^+$ (1−0) (*top*) and C^{18}O (2−1) (*bottom*) emission from the PdBI (*left*), combined (*middle*), and 30m (*right*) datasets for L1448-2A. The blue and red solid arrows represent the directions of the blue- and red-shifted outflow lobes, respectively. The white crosses represent the positions of the binary system determined from the 1.3 mm dust continuum emission (see Table 1). The black cross represents the middle position between the binary system. The clean beam is shown by an ellipse on the bottom left. The integrated intensity contours in black are the same as in Fig. 1.

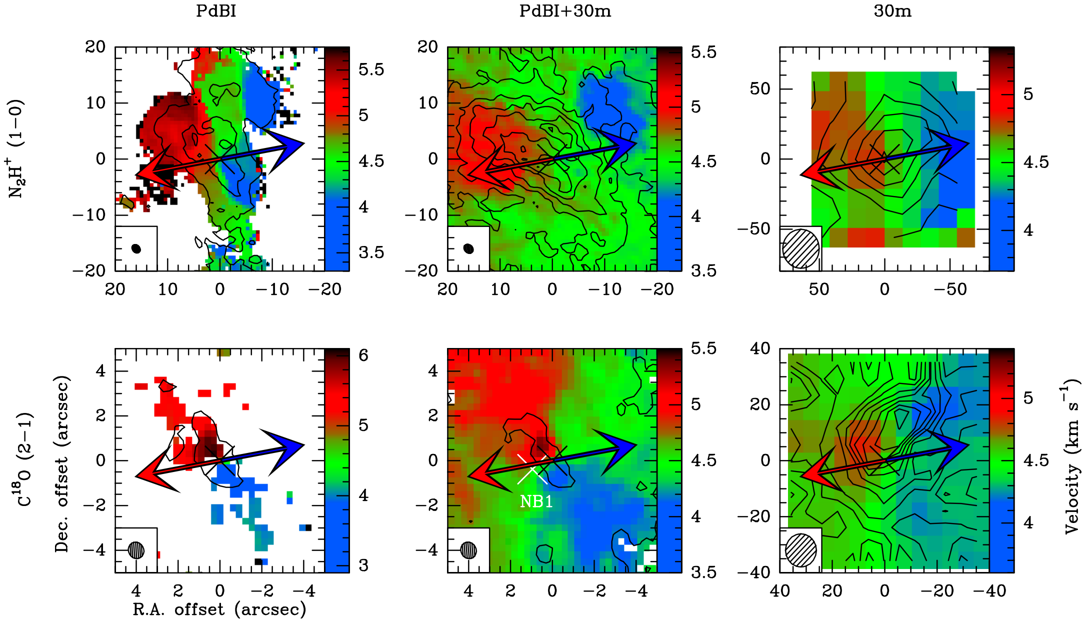

Fig. 4. Same as Fig. 3, but for L1448-NB. The white cross represents the position of main protostar L1448-NB1 determined from the 1.3 mm dust continuum emission (see Table 1). The black cross represents the position of the secondary protostar L1448-NB2 of the multiple system.

to rotational motions and minimize potential contamination on the line of sight due to collapsing or outflowing gas (Yen et al. 2013). The velocities reported in the PV$_{\rm rot}$ diagram are corrected for the inclination i of the equatorial plane with respect to the line of sight (see Table 1). We note that the correction for inclination is a multiplicative factor, thus if this inclination angle is not correctly estimated, the global observed shape is not distorted.

The analysis described in detail in Appendix C allows us to build a PV$_{\rm rot}$ diagram with a high dynamic range from 50 au up to 5000 au for each source as follows (see the example of L1527 in Fig. 15):

Firstly, to constrain the PV$_{\rm rot}$ diagram at the smallest scales resolved by our dataset (~0.5″), we use the PdBI C^{18}O datasets that we analyze in the (u,v) plane to avoid imaging and deconvolution processes (see label "C^{18}O PdBI" in Fig. 15). We only kept central emission positions in the channel maps at a position angle <|45°| with respect to the equatorial axis (see Appendix C).

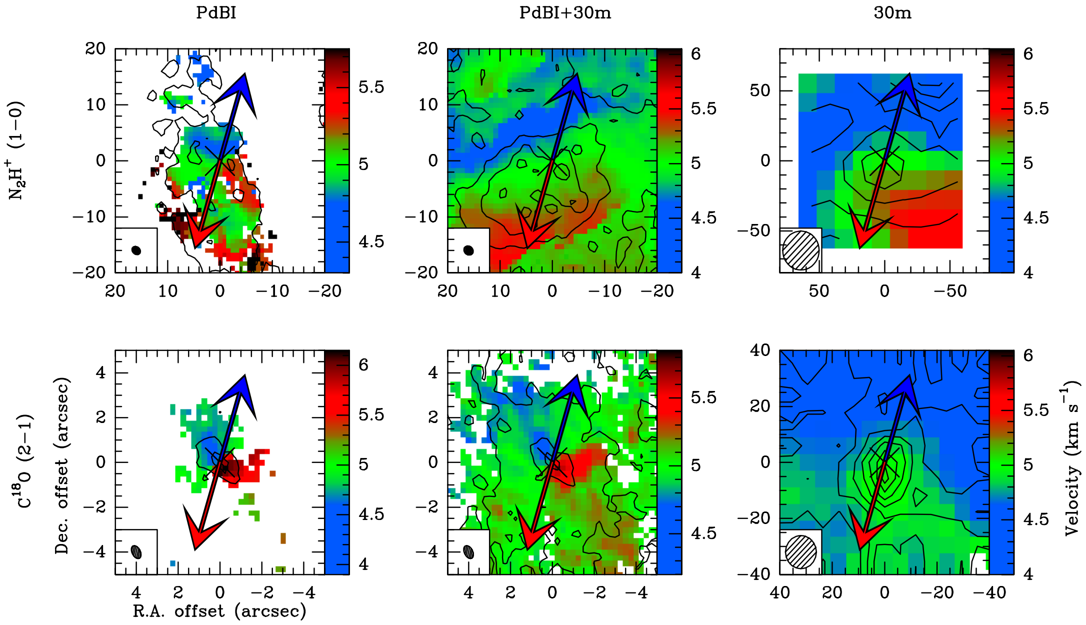

Fig. 5. Same as Fig. 3, but for L1448-C.

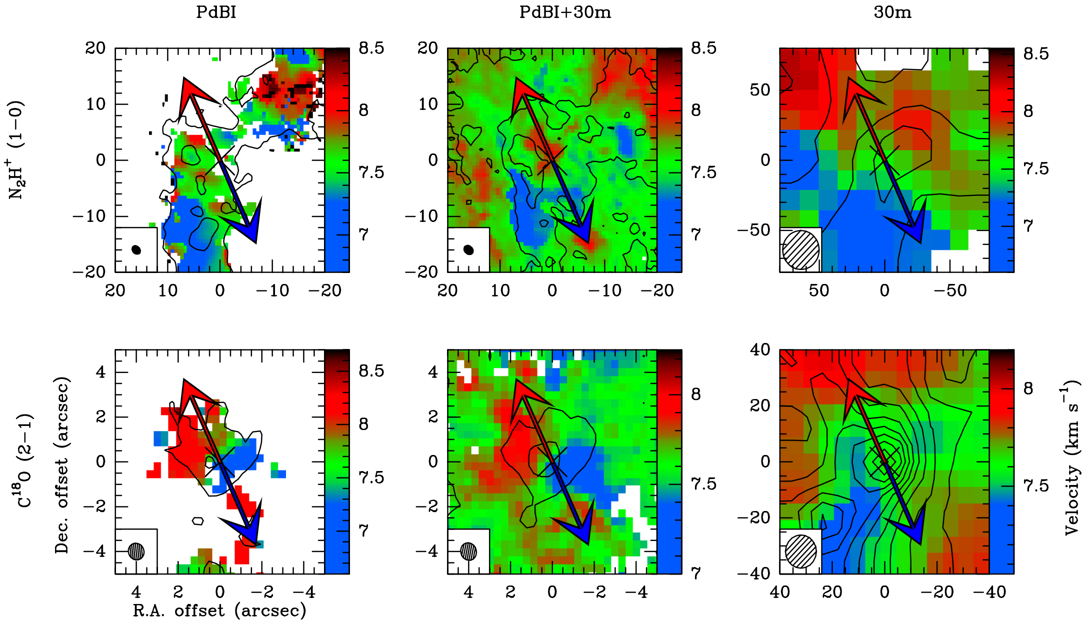

Fig. 6. Same as Fig. 3, but for IRAS2A.

Secondly, since the C^{18}O extended emission is filtered out by the interferometer, we used the combined C^{18}O emission to populate the PV$_{\rm rot}$ diagram at the intermediate scales of the protostellar envelopes (see label "C^{18}O combined" in Fig. 15). The C^{18}O molecule remains the most precise tracer when the temperature is higher than ~20 K because below, the C^{18}O molecule freezes onto dust ice mantles. To determine the transition radius $R_{\rm trans}$ between the two tracers, we calculate the C^{18}O and N$_2$H$^+$ column densities along the equatorial axis from the combined integrated intensity maps (see Appendix D and green points in Fig. 15).

Then, at radii $r > R_{\rm trans}$, the N$_2$H$^+$ emission traces better the envelope dense gas. We use the combined N$_2$H$^+$ emission maps to analyze the envelope kinematics at larger intermediate scales. When the N$_2$H$^+$ column density profile reaches a minimum value due to the sensitivity of the combined dataset, this dataset is no longer the better dataset to provide a robust information on the velocity (see label "N$_2$H$^+$ combined" in Fig. 15).

Finally, we use the 30m N$_2$H$^+$ emission map to populate the PV$_{\rm rot}$ diagram at the largest scales of the envelope (see label "N$_2$H$^+$ 30m" in Fig. 15).

The CALYPSO datasets allow us to continuously estimate the velocity variations along the equatorial axis in the envelope over scales from 50 au up to 5000 au homogeneously for each protostar. Figure 16 shows the PV$_{\rm rot}$ diagrams built for all sources

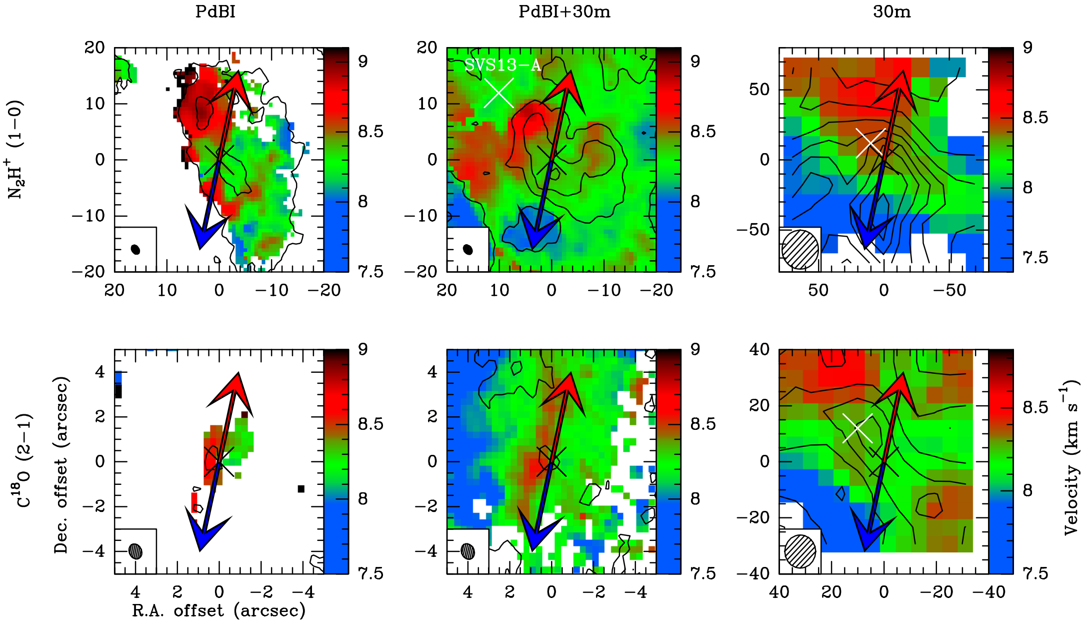

Fig. 7. Same as Fig. 3, but for SVS13-B. The white cross represents the position of the Class I protostar SVS13-A determined from the 1.3 mm dust continuum emission (Maury et al. 2019).

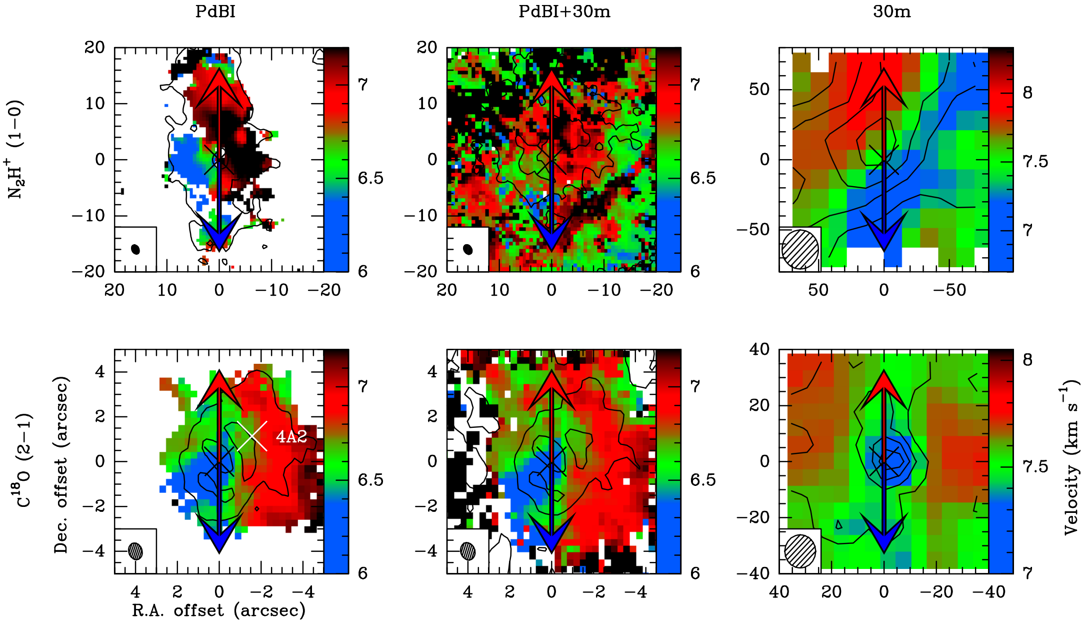

Fig. 8. Same as Fig. 3, but for IRAS4A. The white cross represents the position of secondary protostar IRAS4A2 determined from the 1.3 mm dust continuum emission (see Table 1). The black cross represents the position of the main protostar IRAS4A1 of the multiple system.

of the sample. The systemic velocity used in the PV$_{\rm rot}$ diagrams are determined in Appendix E.

The method of building PV$_{\rm rot}$ diagrams described above and in Appendix C corresponds to an ideal case with a detection of a continuous blue-red velocity gradient along the direction perpendicular to the outflow axis in the velocity maps. In practice, the direction of velocity gradients is not always continuous at all scales probed by our observations (see Table 2 and Fig. 19). For some sources, to constrain the PV$_{\rm rot}$ diagrams, we did not take the kinematic information at all scales of the envelope into account. Velocity gradients can be considered as probing rotational motions if the following criteria are met:

Firstly, we only consider the significant velocity gradients reported in Table 2 with a blue- and a red-shifted velocity components observed on each side of the protostellar embryo, itself at the systemic velocity v_0. For example, we only take the C^{18}O emission from the 30m map into account for L1521F (see Fig. 11).

Secondly, we only take the velocity gradients aligned with the equatorial axis ($\Delta\Theta < 60°$) into account in order to minimize

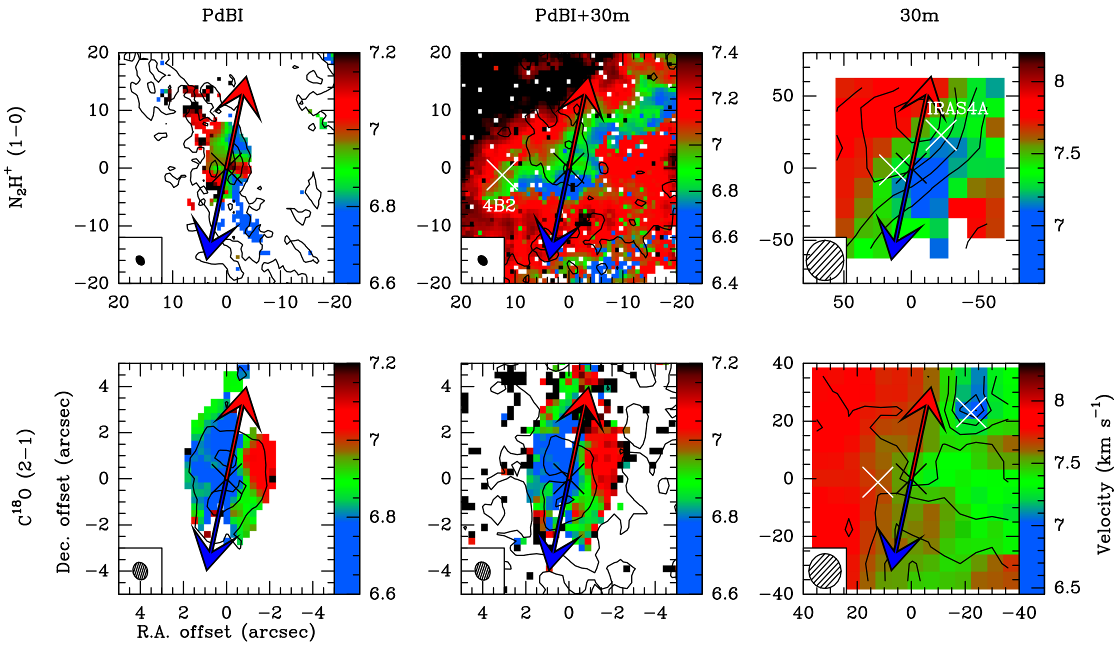

Fig. 9. Same as Fig. 3, but for IRAS4B. The white crosses represent the position of secondary protostar IRAS4B2 and the position of IRAS4A, respectively, determined from the 1.3 mm dust continuum emission (see Table 1). The black cross represents the position of the secondary protostar L1448-NB2 of the multiple system.

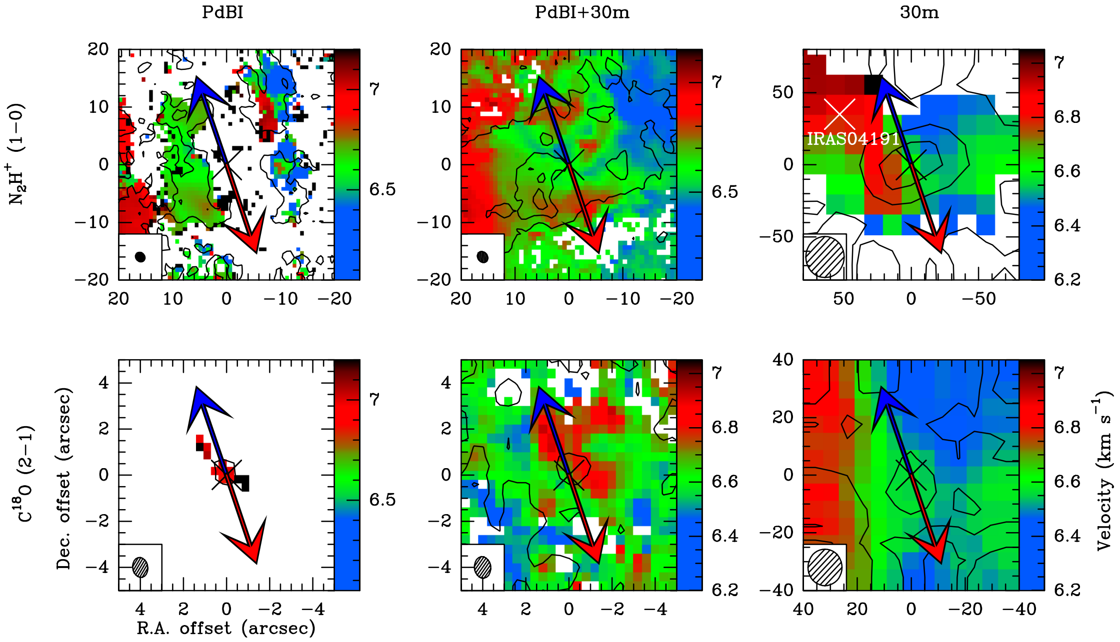

Fig. 10. Same as Fig. 3, but for IRAM04191. The white cross represents the position of the Class I protostar IRAS 04191. The black cross represents the position of IRAM04191 determined from the 1.3 mm dust continuum emission (see Table 1).

contamination by infall and ejection motions. For example, we do not report in the PV$_{rot}$ diagrams the N$_2$H$^+$ velocity gradients from the combined maps for L1448-NB, IRAS2A, SVS13-B, and GF9-2 (see Table 2).

Finally, we do not consider the discontinuous velocity gradients which show an inversion of the blue- and red-shifted velocity components along the equatorial axis from inner to outer envelope scales. For example, we do not report in the PV$_{rot}$ diagrams the N$_2$H$^+$ velocity gradients from the 30m maps for IRAM04191 and L1157 (see Figs. 10 and 13).

When velocity gradients with a blue- and a red-shifted velocity components observed on each side of the protostellar embryo are continuous from inner to outer envelope scales but shifted from the equatorial axis ($\Delta\Theta \geq 60°$), we only report upper limits on rotational velocities in the PV$_{rot}$ diagrams. The sources in our sample show specific individual behaviors, therefore we

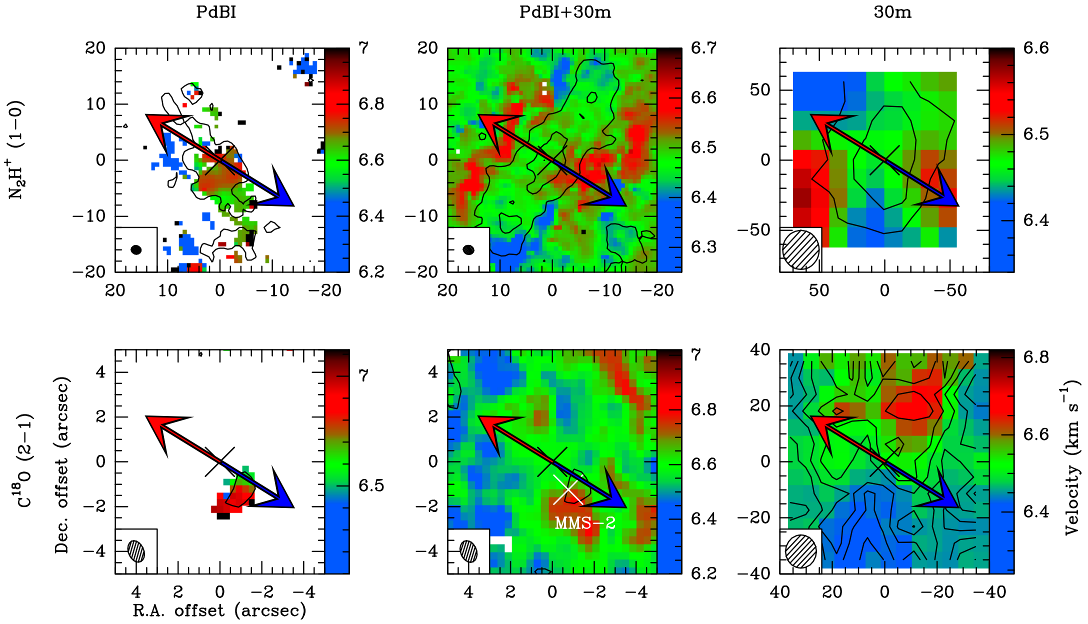

Fig. 11. Same as Fig. 3 for L1521F. The white cross represents the position of the starless dense core MMS-2.

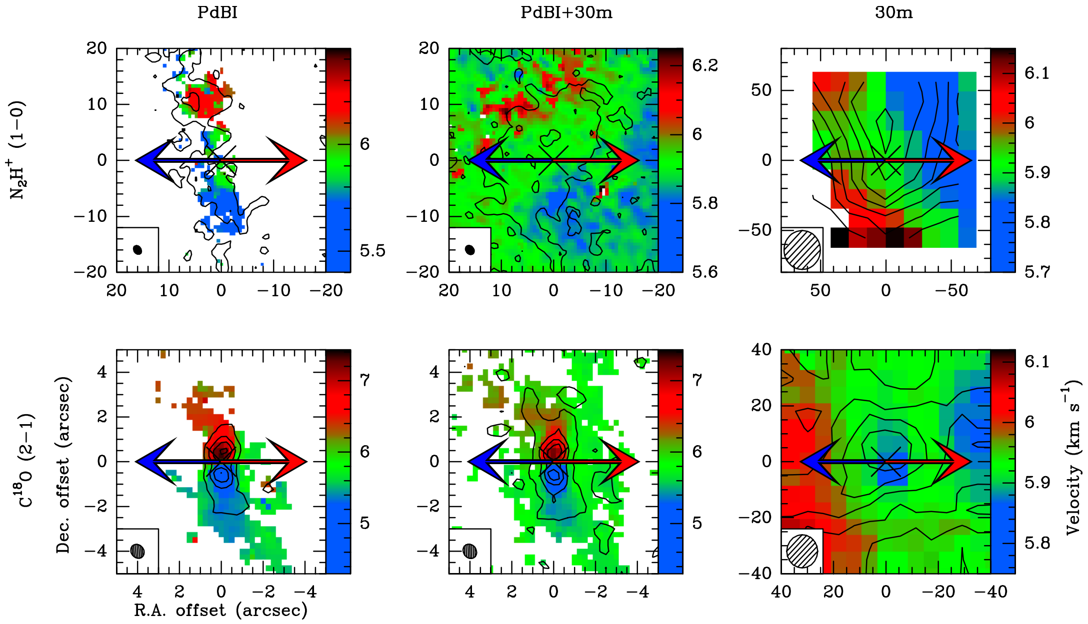

Fig. 12. Same as Fig. 3, but for L1527.

followed as closely as possible the method of building the PV_{rot} diagram adapting it on a case-by-case basis.

5. Discussion

In this section, we discuss the presence of rotation in the protostellar envelopes from the PV_{rot} diagrams (see Sect. 5.1 and Fig. 16). We build the distribution of specific angular momentum associated with the PV_{rot} diagrams (see Sect. 5.2) and explore the possible solutions to explain the $j(r)$ profiles observed in the inner ($r < 1600$ au, see Sect. 5.3) and outer ($r > 1600$ au, see Sect. 5.4) parts of the envelopes.

5.1. Characterization of rotational motions

We assume that the protostellar envelopes are axisymmetric around their rotation axes, and thus, the velocity gradients observed along the equatorial axis, and reported in the PV_{rot} diagrams, are mostly due to the rotational motions of the envelopes. We model the rotational velocity variations by a simple power-law model $v \propto r^{\alpha}$ without taking the upper limits into account. This method has been tested with an axisymmetric model of collapsing-rotating envelopes by Yen et al. (2013). As long as rotation dominates the velocity field on the line of sight, which depends on the inclination and flattening of the envelope, Yen et al. (2013) obtain robust estimates of the rotation motions at

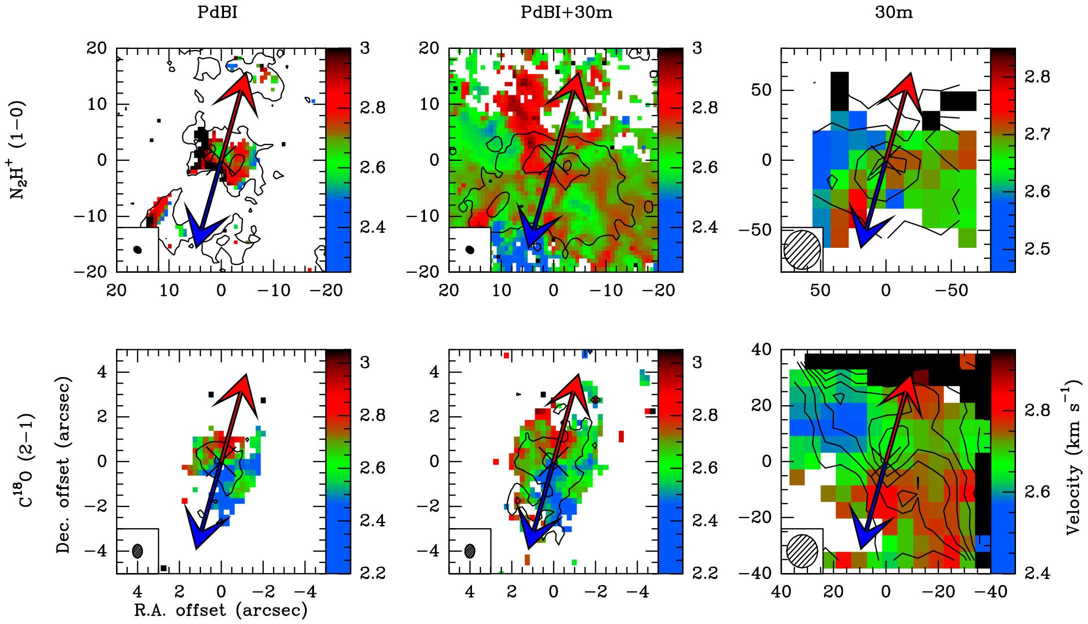

Fig. 13. Same as Fig. 3, but for L1157.

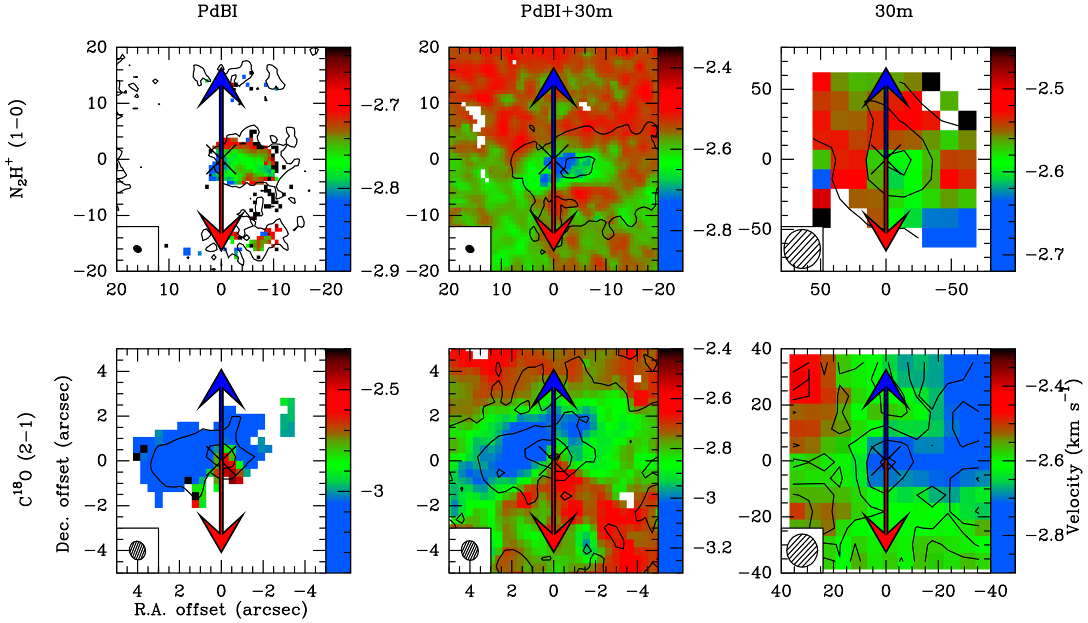

Fig. 14. Same as Fig. 3, but for GF9-2.

work in the envelopes. First, we fix the power-law index at $\alpha = -1$ to compare to what is theoretically expected for an infalling and rotating envelope from a progenitor core in solid-body rotation (Ulrich 1976; Cassen & Moosman 1981; Terebey et al. 1984; Basu 1998). The reduced χ^2 values of fits by an orthogonal least-square model are reported in the second column of Table 3. Then, we let the power-law index vary as a free parameter: the best power-law index and the reduced χ^2 found for each protostellar envelope in our sample are reported in the third column of Table 3. Figure 16 shows the PV$_{\rm rot}$ diagrams adjusted by a power-law for the sources of the CALYPSO sample.

The power-law indices of the PV$_{\rm rot}$ diagrams from our sample are between −1.1 and 0.8. Five sources (L1448-2A, IRAS2A, SVS13-B, L1527, and GF9-2) show rotational velocity variations in the envelope scaling as a power law with an index close to −1. This is consistent with the expected index for collapsing and rotating protostellar envelopes. The reduced χ^2 are ~1.5 for these sources except for IRAS2A and SVS13-B for which it is better (~0.2). L1521F and L1157 show a power-law index close to 0 with a very low reduced χ^2 (≤0.3, see Table 3). These flat PV$_{\rm rot}$ diagrams ($v_{\rm rot} \sim$ constant) suggest differential rotation of the envelope with an angular velocity of $\Omega = \frac{v_{\rm rot}}{r} \propto r^{-1}$. For two other sources (IRAS4B and IRAM04191), the best indices are compatible with −0.5, which could suggest Keplerian rotation at scales of $r < 1000$ au. However, the reduced χ^2 are also satisfactory (~1) when we fix the power-law index at $\alpha = -1$

Table 2. Estimation of the systemic velocity, the mean velocity gradient amplitude and its orientation from linear gradient fit of centroid velocity maps in $C^{18}O$ and N_2H^+ emission from the PdBI, the combined, and the 30m datasets for the CALYPSO sample sources.

Source	Line	PdBI				PdBI+30m				30m			
		G (km s^{-1} pc^{-1})	v_0 (km s^{-1})	$\Theta^{(a)}$ (°)	$\Delta\Theta^{(b)}$ (°)	G (km s^{-1} pc^{-1})	v_0 (km s^{-1})	$\Theta^{(a)}$ (°)	$\Delta\Theta^{(b)}$ (°)	G (km s^{-1} pc^{-1})	v_0 (km s^{-1})	$\Theta^{(a)}$ (°)	$\Delta\Theta^{(b)}$ (°)
L1448-2A	$C^{18}O$ (2-1)	118 ± 3	4.06 ± 0.03	107 ± 2	69	13 ± 2	4.05 ± 0.04	81 ± 1	43	6 ± 1	4.12 ± 0.02	−14 ± 2	52
	N_2H^+ (1-0)	19 ± 1	4.09 ± 0.03	−89 ± 2	53	2 ± 1	4.10 ± 0.04	−177 ± 21	35	2 ± 1	4.16 ± 0.04	−8 ± 3	46
L1448-NB	$C^{18}O$ (2-1)	214 ± 1	4.71 ± 0.06	51 ± 1	41	75 ± 1	4.55 ± 0.05	50 ± 1	40	6 ± 1	4.45 ± 0.02	85 ± 4	75
	N_2H^+ (1-0)	108 ± 1	4.55 ± 0.02	74 ± 1	64	13 ± 1	4.57 ± 0.02	100 ± 1	90	4 ± 1	4.51 ± 0.01	97 ± 1	87
L1448-C	$C^{18}O$ (2-1)	218 ± 4	5.13 ± 0.05	−119 ± 2	12	62 ± 1	5.03 ± 0.05	−138 ± 1	31	–	–	–	–
	N_2H^+ (1-0)	15 ± 2	4.92 ± 0.03	−175 ± 4	68	13 ± 1	4.97 ± 0.03	−179 ± 1	72	7 ± 1	4.85 ± 0.01	−152 ± 1	45
IRAS2A	$C^{18}O$ (2-1)	150 ± 5	7.75 ± 0.08	101 ± 2	14	17 ± 1	7.63 ± 0.06	97 ± 3	18	3 ± 1	7.66 ± 0.01	−10 ± 1	55
	N_2H^+ (1-0)	11 ± 1	7.57 ± 0.04	−20 ± 6	45	4 ± 1	7.64 ± 0.03	20 ± 4	85	5 ± 1	7.61 ± 0.01	−5 ± 1	60
SVS13-B	$C^{18}O$ (2-1)	–	–	–	–	28 ± 4	8.19 ± 0.08	89 ± 10	12	7 ± 1	8.15 ± 0.02	−33 ± 1	70
	N_2H^+ (1-0)	16 ± 1	8.48 ± 0.03	74 ± 1	3	5 ± 1	8.31 ± 0.02	16 ± 4	61	7 ± 1	8.07 ± 0.02	−4 ± 1	81
IRAS4A	$C^{18}O$ (2-1)	105 ± 1	6.57 ± 0.04	−79 ± 1	11	18 ± 4	6.72 ± 0.06	−80 ± 17	10	1.2 ± 0.4	7.57 ± 0.04	8 ± 13	82
	N_2H^+ (1-0)	43 ± 1	6.85 ± 0.05	−69 ± 1	21	7 ± 1	6.90 ± 0.06	37 ± 2	53	3 ± 1	7.48 ± 0.02	51 ± 1	39
IRAS4B	$C^{18}O$ (2-1)	65 ± 1	6.84 ± 0.03	−89 ± 1	14	52 ± 5	6.89 ± 0.06	−83 ± 8	20	–	–	–	–
	N_2H^+ (1-0)	25 ± 2	6.94 ± 0.04	96 ± 6	19	3 ± 1	7.06 ± 0.05	−71 ± 14	32	3 ± 1	7.47 ± 0.02	51 ± 5	27
IRAM04191	$C^{18}O$ (2-1)	–	–	–	–	25 ± 2	6.62 ± 0.07	−42 ± 5	28	6 ± 1	6.59 ± 0.01	96 ± 1	14
	N_2H^+ (1-0)	11 ± 2	6.76 ± 0.05	109 ± 3	1	15 ± 1	6.64 ± 0.03	92 ± 1	18	3 ± 1	6.61 ± 0.01	124 ± 1$^{(\star)}$	14
L1521F	$C^{18}O$ (2-1)	–	–	–	–	16 ± 1	6.57 ± 0.04	−82 ± 2	52	2 ± 1	6.49 ± 0.01	−8 ± 1	22
	N_2H^+ (1-0)	26 ± 2	6.67 ± 0.04	−76 ± 5	46	0.7 ± 0.1	6.48 ± 0.01	−49 ± 2	19	0.4 ± 0.1	6.47 ± 0.01	6 ± 2	36
L1527	$C^{18}O$ (2-1)	171 ± 5	5.91 ± 0.06	−9 ± 3	9	66 ± 1	5.84 ± 0.06	22 ± 2	22	2 ± 1	5.94 ± 0.01	113 ± 1	67
	N_2H^+ (1-0)	17 ± 1	5.87 ± 0.03	9 ± 6	9	3 ± 1	5.91 ± 0.02	26 ± 5	26	2 ± 1	5.91 ± 0.01	123 ± 4	57
L1157	$C^{18}O$ (2-1)	104 ± 3	2.61 ± 0.06	13 ± 2	60	68 ± 2	2.63 ± 0.06	35 ± 2	38	2 ± 1	2.70 ± 0.15	−125 ± 8	18
	N_2H^+ (1-0)	51 ± 2	2.82 ± 0.04	35 ± 2	38	0.8 ± 0.4	2.69 ± 0.02	113 ± 65	40	1.0 ± 0.5	2.65 ± 0.04	−131 ± 35	24
GF9-2	$C^{18}O$ (2-1)	126 ± 17	−3.01 ± 0.06	−154 ± 4	64	17 ± 1	−2.83 ± 0.03	−133 ± 5	43	2 ± 1	−2.62 ± 0.01	102 ± 1	12
	N_2H^+ (1-0)	18 ± 3	−2.80 ± 0.01	−123 ± 8	33	1.4 ± 0.1	−2.56 ± 0.01	−9 ± 5	81	0.5 ± 0.1	−2.56 ± 0.01	40 ± 8	50

Notes. $^{(a)}$Position angle of the redshifted lobe of the velocity gradient defined from north to east. $^{(b)}$Absolute value, between 0° and 90°, of the difference between the angle of the mean gradient and the angle of the equatorial axis. The equatorial axis is defined perpendicularly to the direction of the outflows (see Table 1). $^{(\star)}$For IRAM04191, the N_2H^+ emission in the 30m dataset was fit ignoring the pixels close to the Class I protostar IRAS 04191 in the field of view (see Appendix H).

(see Table 3). Thus, for these two sources, our CALYPSO datasets only allow us to estimate a range of the power-law indices between −1 and −0.5 (see Table 3).

Rotational velocity variations along the equatorial axis between 50 and 5000 au in L1448-NB cannot be reproduced satisfactorily by any single power-law model ($\chi^2 > 2$, see Table 3). However, considering only the points at $r < 400$ au for L1448-NB, we obtain a power-law index of −0.9±0.2 with a good reduced χ^2 of 0.4, as expected for a collapsing and rotating envelope (see Table 3).

We found a positive index α for IRAS4A of 0.8 (see Table 3). It could be an indication of solid-body rotation of $\Omega = \frac{v_{\rm rot}}{r} \sim$ constant. However, we observe that the velocity in the $PV_{\rm rot}$ diagram decreases from 2000 to ~600 au and re-increases at small scales (see panel f of Fig. 16). Thus, the velocity gradient is not uniform on the scales traced by the $PV_{\rm rot}$ diagram as would be expected for a solid-body rotation ($v_{\rm rot} \propto r$). Moreover, points at radii <600 au are consistent with an infalling and rotating envelope (see panel f of Fig. 16): considering only these points, we obtain a power-law index of -1.3 ± 0.6 with a good reduced χ^2 value of 0.6 (see Table 3). There is a dip in the $C^{18}O$ emission at $r < 350$ au that could be due to the opacity (see Figs. H.20 and H.19), thus, below this radius the information on velocities could be altered. To date, no observations have identified any solid-body rotating protostellar envelope. Numerical models also favor differential rotation of the envelope (Basu 1998). The interpretation of the velocity field as tracing solid-body rotation in the envelope of IRAS4A is therefore unlikely to be correct.

For the sources IRAS2A, IRAM04191, and L1157, the reduced χ^2 is also good (~1) when the $PV_{\rm rot}$ diagrams of these sources are ajusted by a model with a fixed index of $\alpha = -1$ (see Table 3). We determine position and velocity from four different and independent methods and we did not consider the uncertainties of the connection between the different tracers and datasets. The uncertainty on the indices reported in Table 3 may thus be underestimated. On the other hand, although we determined the systemic velocity by maximizing the overlap of the blue and red points, this method does not allow a more accurate determination than 0.05 km s^{-1}. The systematic error of 0.05 km s^{-1}, added to previous velocity errors of the points in the $PV_{\rm rot}$ diagrams to take this uncertainty on the systemic velocity into account (see Appendix E), can be overestimated and thus lead us to

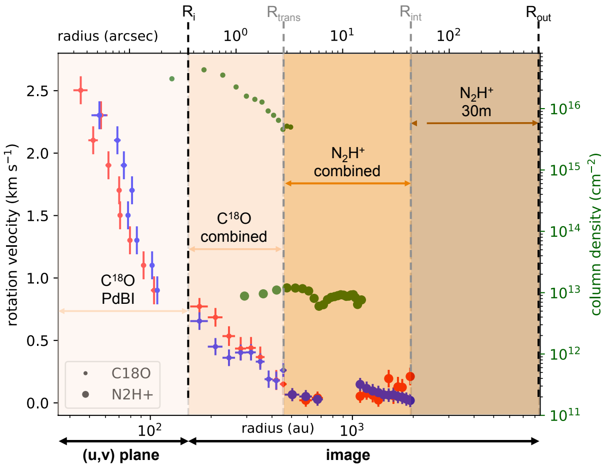

Fig. 15. Summary of the combination of tracers and datasets used to build high dynamic range PV_{rot} diagrams in the L1527 envelope. The transition radii between the different datasets (PdBI, combined, and 30m) and the two $C^{18}O$ and N_2H^+ tracers represented by the dashed lines are given in Table C.1. The green points show the column density profiles along the equatorial axis of $C^{18}O$ and N_2H^+ estimated from the combined datasets (see Appendix D).

Table 3. Parameters of best power-law fits to the PV_{rot} diagrams.

Source	Radial range$^{(a)}$ (au)	Power law fit α=-1$^{(b)}$ DoF	χ^2	Power law fit$^{(c)}$ DoF	α	χ^2
L1448-2A	60−1250	8	1.3	7	−0.9 ±0.1	1.4
L1448-NB	150−1700	34	2.3	33	−0.94 ±0.04	2.3
	150−350	...	...	5	−0.9 ±0.2	0.4
L1448-C	100−4000	19	1.6	18	−1.0 ±0.1	1.7
IRAS2A	85−1500	13	0.9	12	−0.7 ±0.1	0.2
SVS13-B	110−450	7	0.2	6	−0.9 ±0.3	0.2
IRAS4A	250−1600	18	20.4	17	0.8±0.1	1.5
	250−550	...	...	5	−1.3±0.6	0.6
IRAS4B	175−1050	12	0.6	11	−0.6 ±0.3	0.5
IRAM04191	55−800	9	1.1	8	−0.3 ±0.2	0.3
L1521F	1500−4200	6	1.0	5	0.2 ±0.5	0.1
L1527	45−2000	58	1.9	57	−1.13 ± 0.03	1.6
L1157	85−650	10	1.2	9	0.1 ±0.3	0.3
GF9-2	75−850	10	2.0	9	−0.8 ±0.1	1.8

Notes. $^{(a)}$Range of radii over which the PV_{rot} diagrams were built and the fits were performed. $^{(b)}$Number of degrees of freedom we used for the modeling and reduced χ^2 value associated with the best fit with a power-law function v ∝ r^{-1}. $^{(c)}$Number of degrees of freedom we used for the modeling, index of fit with a power-law function ($\upsilon \propto r^{\alpha}$) and the reduced χ^2 value associated with this best fit model.

underestimate the χ^2. For these three sources, the CALYPSO dataset only allow us to estimate a range of power-law indices between −1 and the α value reported in the fifth column of Table 3. The uncertainties on the indices reported in Table E are statistical errors and a systematic uncertainty of ±0.1 has to be added to account for the uncertainties in the outflow directions and thus the equatorial axis directions (see Table 1). Moreover, despite the choice of the equatorial axis, the rotational velocities could be contaminated by infall at the small scales along this axis due to the envelope geometry.

To conclude, the organized motions reported in the PV_{rot} diagrams and modeled by a power-law function with an index α ranging from −2 to 0 are consistent with differential rotational motions ($\Omega \propto r^{\epsilon}$, with $-3 < \epsilon < -1$ here). We identified rotational motions in all protostellar envelopes in our sample except in IRAS4A.

5.2. Distribution of specific angular momentum in the CALYPSO Class 0 envelopes

5.2.1. Specific angular momentum due to rotation motions

Assuming the motions detected along the equatorial axis are dominated by differential rotation for 11 of the 12 sources in our sample, we use the measurements reported in the PV_{rot} diagrams to derive the radial distribution of specific angular momentum in the protostellar envelopes due to rotation. In this part of the study, IRAS4A is excluded. The specific angular momentum is $j = \frac{J}{M} = \frac{I\Omega}{M}$ with the moment of inertia I defined as $I \propto Mr^2$ (Belloche 2013). Thus, the specific angular momentum is calculated from the rotational velocity: $j = \upsilon_{rot}(r) \times r$. We plot all the specific angular momentum profiles obtained for the CALYPSO subsample in panel b of Fig. 17. The individual distribution of specific angular momentum $j(r)$ for each source is given in Appendix H. This is the first time that the specific angular momentum distribution as a function of radius within a protostellar envelope is determined homogeneously for a large sample of 11 Class 0 protostars. We performed a least-square fit of the $j(r)$ profiles for each source individually, using a model of a simple power-law and a broken power-law model to identify the change of regimes. The broken power-law model function is defined with a break radius r_{break} as follows:

$$j(r) \propto \left(\frac{r}{r_{break}}\right)^{\beta_1} \quad \text{when} \quad r < r_{break},$$

$$j(r) \propto \left(\frac{r}{r_{break}}\right)^{\beta_2} \quad \text{when} \quad r > r_{break}.$$

We report in Table F.1 the power-law indices fitting the best individual profiles and the associated reduced χ^2. For the broken power-law fits, only results with a reduced χ^2 better than the one obtained with a simple power-law model and with a break radius value r_{break} to which the $j(r)$ profile is really sensitive, have been retained.

Two sources (L1448-NB and L1448-C) are better reproduced by a broken power-law model than a simple power-law model where the χ^2 are ∼2: this allows us to identify a change of slope from a relatively flat profile to an increasing profile at larger radius in the envelope ($\beta \sim 1$), with break radii between 500 and 700 au. For the other sources, we also identified at scales of $r < 1300$ au a flat profile of specific angular momentum with $\beta < 0.5$ (L1448-2A, IRAS2A, SVS13-B, IRAS4B, L1527, and GF9-2) while the specific angular momentum profile at scales of $r > 1000$ au shows a steeper slope with $\beta \sim 1$ (L1521-F). However, two sources of the sample (IRAM04191 and L1157) stand out as the sources showing a steep increase in their specific angular momentum profile at scales of $r < 1000$ au ($\beta \geq 0.7$), similar to the indices found at large radii in the sources showing

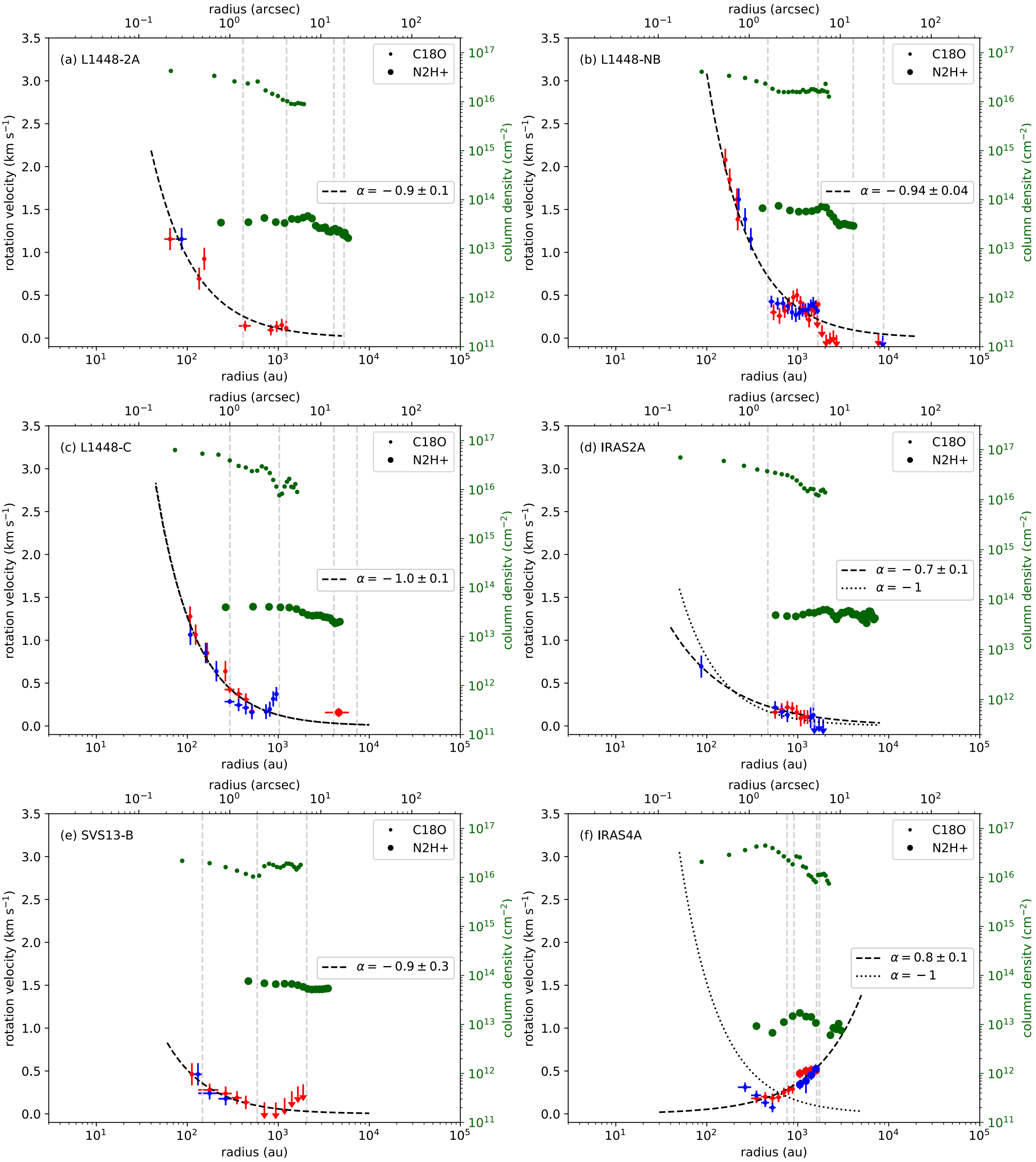

Fig. 16. Position-velocity diagram along the equatorial axis of the CALYPSO protostellar envelopes. Blue and red dots show the blue- and red-shifted velocities, respectively. The arrows display the upper limits of $v_{\rm rot}$ determined from velocity maps that do not exhibit a spatial distribution of velocities as organized as one would expect from rotation motions (see Sect. 4.3 and Appendix C). Green dots show the column density profiles along the equatorial axis. Dots and large dots show the C^{18}O and N$_2$H$^+$ data, respectively. The dashed curve shows the best fit with a power-law model leaving the index α as a free parameter ($v_{\rm rot} \propto r^{\alpha}$) whereas the dotted curve shows the best fit with a power-law model with a fixed index $\alpha = -1$. The vertical dashed lines show the transition radii between the different datasets (PdBI, combined, and 30m) and the two tracers as illustrated in Fig. 15 and given in Table C.1.

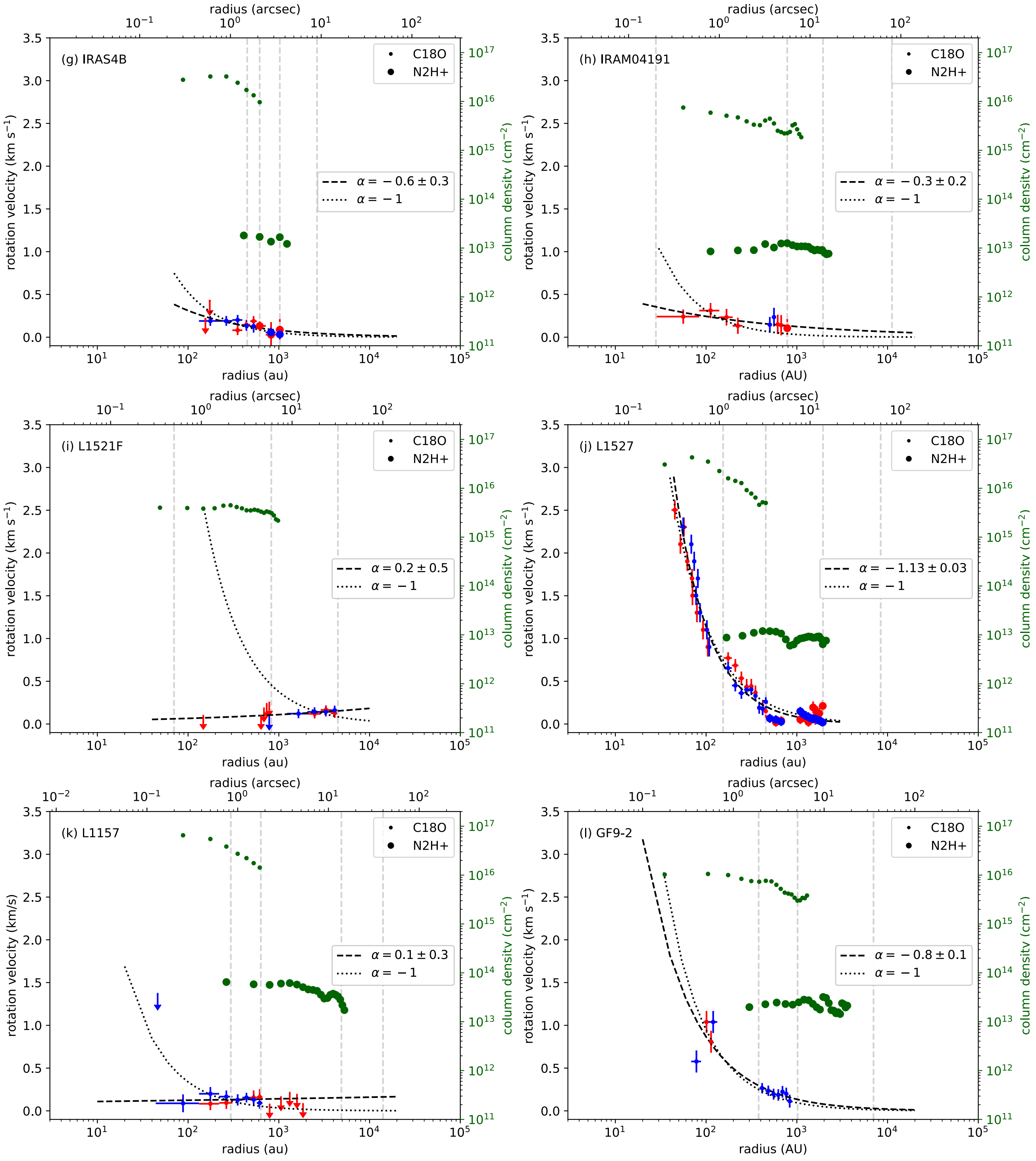

Fig. 16. continued.

a break in their $j(r)$ profiles. We note that for the flat profiles ($\beta < 0.5$; L1448-2A, SVS13-B, IRAS4B, and GF9-2), and IRAM04191 and L1157, the specific angular momentum distribution is only constrained at scales < 1300 au. Most of the sources in our sample are better reproduced by a broken power-law model with a break radius (1000 ± 500) au and an increasing profile at larger radius in the envelope ($\beta \sim 1.4$) than a simple power-law model.

In his review, Belloche (2013) plotted the observed specific angular momentum as a function of rotation radius for several objects along the star-forming sequence. In this plot (panel a of Fig. 17), he identifies three regimes in the distribution of specific angular momentum, that can be broadly associated with different evolutionary stages. During the prestellar regime, on large scales, the apparent angular momentum of molecular clouds (Goldsmith & Arquilla 1985) and dense cores

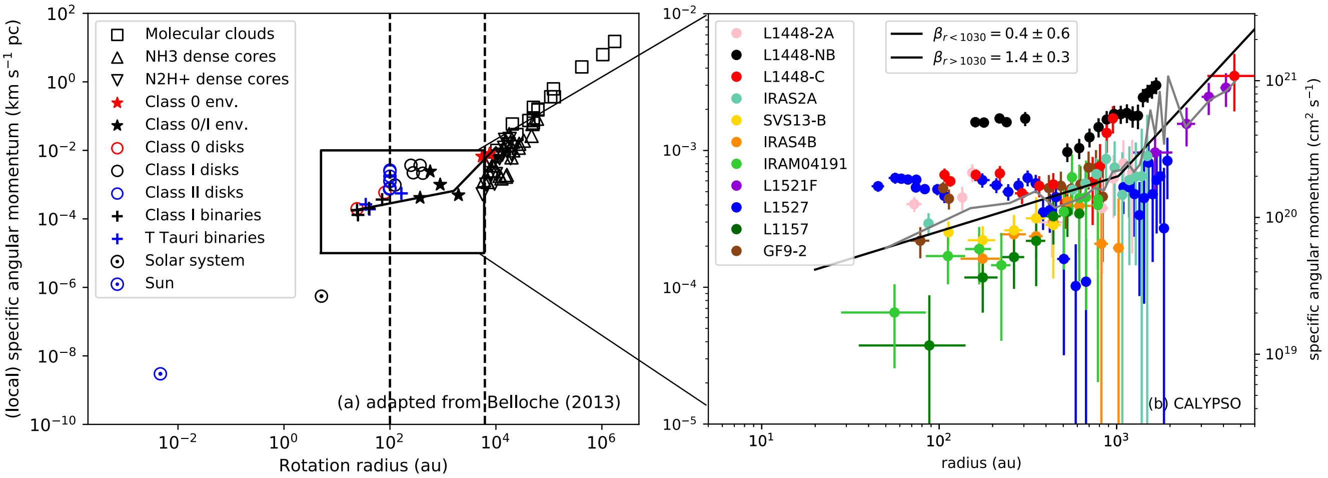

Fig. 17. Radial distribution of specific angular momentum. *Panel a*: adapted from Fig. 8 of Belloche (2013) and from Ohashi et al. (1997a). *Panel b*: zoom on the region where the angular momentum profiles due to rotation of the CALYPSO sources lie. The gray curve shows the median profile $j(r)$. In the two panels, the solid black line shows the best fit with a broken power-law model.

(Goodman et al. 1993; Caselli et al. 2002) appears to follow the power-law relation $j \propto r^{1.6}$. During protostellar regime, between 100 and ~6000 au (0.03 pc), a few points in different protostellar envelopes suggest the specific angular momentum is relatively constant ($j \sim 10^{-3}$ km s^{-1} pc, Ohashi et al. 1997a; Belloche et al. 2002; Chen et al. 2007). During disk and binary regime, below 100 au, measurements in disks and Class II binaries (Chen et al. 2007) show a decrease of j following a trend characteristic of Keplerian rotation ($j \propto r^{0.5}$).

Thus, from previous observational studies on rotational motions, finding a break at $r \sim 1000$ au between two trends of specific angular momentum within Class 0 protostars was unexpected. Although the velocity gradients observed in the outer part of the protostellar envelopes ($r > 1000$ au) are consistent with rotational motions, the observed j regime at these scales is not expected from pure rotational motions.

5.2.2. Apparent specific angular momentum

The radius range of $j(r)$ distribution due to rotation motions is not homogeneous between sources (see Table F.1). To identify whether the radius of ~1000 au is a critical radius between two trends of specific angular momentum in each source, we derive the radial distribution of the apparent specific angular momentum $|j_{\rm app}|$ at all scales in the envelopes. To build $|j_{\rm app}|(r)$ distribution, we consider the gradients observed at all envelope scales, including also the reversed gradients and the shifted ones at scales of $r \gtrsim 1000$ au (see Fig. 19 and Sect. 5.4) which were excluded in the construction of the PV$_{\rm rot}$ diagrams in Fig. 16 because they are not consistent with rotational motions. By considering these velocity gradients, we add points in the outer envelopes but the trend observed in the inner envelopes do not change (see Tables F.1 and F.2). Thus, the $|j_{\rm app}|(r)$ distribution helps us to understand the origin of the trend and the velocity gradients observed at $r > 1000$ au. We plot all the apparent specific angular momentum profiles obtained for the CALYPSO subsample in Fig. 18. We also report the apparent specific angular momentum of IRAS4A which was identified as the only source that did not show any rotational motions in our sample (see Sect. 5.1). As for j profiles, we performed a least-square fit of the $|j_{\rm app}|(r)$ profiles for each source individually and we report the indices of the power-law models in Table F.2.

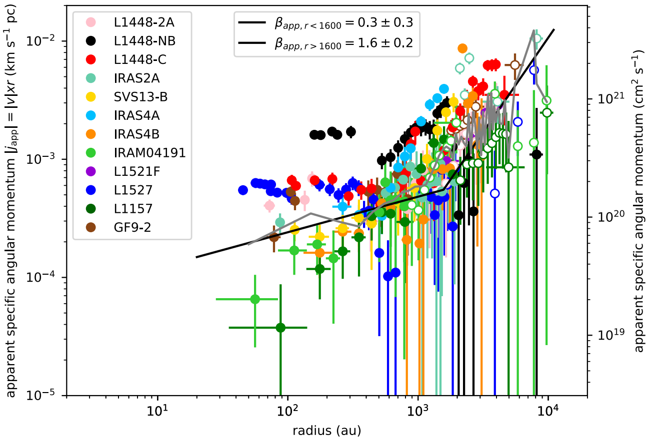

Fig. 18. Radial distribution of apparent specific angular momentum $|j_{\rm app}| = |v| \times r$ along the equatorial axis of the CALYPSO sources, considering all the velocity gradients observed at all envelope scales, including the reversed gradients and the shifted ones at scales of $r \gtrsim 1600$ au (see Fig. 19 and Sect. 5.4) which were excluded in the construction of the PV$_{\rm rot}$ diagrams in Fig. 16, and in panel b of Fig. 17 for our analysis of rotational motions. The empty circles show the negative apparent specific angular momentum from the reversed gradients along the equatorial axis in the outer scales ($r > 1600$ au) of the L1448-2A, IRAS2A, IRAM04191, L1527, L1157 and GF9-2 envelopes (see Sect. 5.4.1). The gray curve shows the median profile $|j_{\rm app}|$ and the solid black line shows the best fit with a broken power-law model.

We create the median $|j_{\rm app}|(r)$ profile of the CALYPSO subsample. We first resampled the individual profile of each source in steps of 100 au and normalized it by the value at 600 au, then we took the median value of individual profiles at each radius step. The median profile is shown in gray on Fig. 18. From a broken power-law fit, we obtain a relatively flat profile ($j_{\rm app} \propto r^{0.3\pm0.3}$) at radii smaller than 1570±300 au and an increasing profile ($j_{\rm app} \propto r^{1.6\pm0.2}$) in the outer envelope. The radius of ~1600 au therefore appears to be a critical radius which delimits two regimes of angular momentum in protostellar envelopes: the specific angular momentum decreases down to ∼1600 au and then tends to become constant.

The change of behavior of $j_{\rm app}$ above the break radius could be due to a change of tracer to study the kinematics in the outer envelope. However, we do not find any systematic consistency between $r_{\rm app,break}$ and the transition radius $R_{\rm trans}$ between the two tracers $C^{18}O$ and N_2H^+. Even if for SVS13-B, $R_{\rm trans}$ is in the error bars of $r_{\rm app,break}$, for three sources (L1448-NB, L1448-C, and IRAS4A) it is not consistent, and for IRAS4B, we do not observe a change of regime for $j_{\rm app}$ at r ∼1600 au (see Tables F.1 and F.2). Moreover, for L1521F, only the $C^{18}O$ emission shows a velocity gradient allowing us to constrain the kinematics at scales of $r > 1600$ au (see Fig. 11) and we find the same trend of $j_{\rm app}$ ($\beta_{\rm app}$ ∼1.2) than in all other sources where we used N_2H^+ to constrain the outer part of the envelopes. The other sources (L1448-2A, IRAS2A, IRAM04191, L1527, L1157, and GF9-2) show a negative value of the apparent angular momentum at outer envelope scales due to a renversal of the velocity gradients (see Fig. 18, Table F.2, and Sect. 5.4.1). For two of these sources (L1448-2A and GF9-2) the radius where the gradient reverses along the equatorial axis, resulting in a negative $j_{\rm app}$ with respect to the inner envelope scales, is consistent with $R_{\rm trans}$ and $r_{\rm app,break}$. For two sources (IRAS2A and IRAM04191), $R_{\rm trans}$ is consistent with the radius where the gradient reverses along the equatorial axis but not with $r_{\rm app,break}$. For the last two sources (L1527 and L1157), the three radii are all different from each other. The different individual behaviors in the CALYPSO sample allow us to conclude that our finding that protostellar envelopes are characterized by two regimes of angular momentum does not result from our use of two different tracers.

From the median $|j_{\rm app}|(r)$ profile without normalization of the individual profiles at 600 au, we find a mean value of specific angular momentum in the inner parts of the envelopes ($r < 1600$ au) of ∼6×10^{-4} km s^{-1} pc. This value is slightly lower but compatible with the estimates made by Ohashi et al. (1997a) and Chen et al. (2007) in four Class 0 or I sources (j ∼10^{-3} km s^{-1} pc at $r < 5000$ au). It is also consistent with the studies by Yen et al. (2015a,b) which find values between 5×10^{-3} and 5×10^{-5} km s^{-1} pc in the inner envelope ($r <$ 1500 au). Yen et al. (2015a) estimate a specific angular momentum of ∼5×10^{-4} km s^{-1} pc at r ∼100 au for L1448-C and L1527. Moreover, our values for L1157 are consistent with their upper limit estimate of 5×10^{-5} km s^{-1} pc in the inner envelope ($r <$ 100 au) of L1157.

The high angular resolution and the high dynamic range of the CALYPSO observations allow us to identify the first two regimes within individual protostellar envelopes: values at radii $\gtrsim$1600 au ($j_{\rm app} \propto r^{1.6}$ on average, see Table F.2) seem to correspond to the trend found in dense cores at scales >6000 au while the values stabilize around ∼6×10^{-4} km s^{-1} pc on average at radii <1600 au. This study resolves for the first time the break radius between these two regimes deeper within the protostellar envelopes at around ∼1600 au instead of ∼6000 au. In a study of ammonia emission in the outer envelopes of two Class 0 objects, Pineda et al. (2019) find an increasing angular momentum profile scaling as $r^{1.8}$ from 1000 to 10 000 au, with values ∼3×10^{-4} km s^{-1} pc at radii ∼1000 au. They do not detect the break around ∼1600 au found in the CALYPSO sample. This break radius from which the profiles are found to be flat in the inner envelope may depend on the evolutionary stage of the accretion process during the Class 0 phase as suggested by Yen et al. (2015b). It could be due to the propagation of the inside-out expansion wave during the collapse (Shu 1977): assuming a median lifetime or half life of ∼5×10^4 yr for Class 0 protostar envelopes (Maury et al. 2011; see also Evans et al. 2009) at sound velocity (∼0.2 km s^{-1}), one obtains a radius ∼2000 au. This radius is on the same order of magnitude as the observed break radius between the two regimes observed in the distribution of specific angular momentum of sources in our sample. In this case, the break radius could be an indication of the age of the protostars, except for four sources (L1448-NB, IRAM04191, L1521F, and L1157) in our sample where we do not observe this break radius. Beyond this radius, the outer envelope may not have collapsed yet, and could therefore retain the initial conditions in angular momentum of the progenitor prestellar core.

This could be an explanation for the increase in angular momentum observed at the scales of $r > 1600$ au ($j_{\rm app} \propto r^{1.6}$ on average, see Table F.2), consistent with the prestellar stage ($j \propto r^{1.6}$). We discuss the properties and physical origin of these two regimes in more details in the next sections.

5.3. Conservation of angular momentum in Class 0 inner envelopes

In this section, we focus on the relatively constant values of specific angular momentum observed in the inner envelopes at scales of $r \leq 1600$ au in the $j(r)$ profiles due to rotation motions (see Fig. 17). From these flat profiles, we find that the matter directly involved in the formation of the stellar embryo has a specific angular momentum ∼3 orders of magnitude higher than the one in T-Tauri stars ($j \sim 2 \times 10^{-7}$ km s^{-1} pc, Bouvier et al. 1993). We discuss constant values of specific angular momentum as conservation of angular momentum to test disk formation as a possible solution to the angular momentum problem.

It is difficult to constrain the time evolution of specific angular momentum for a given particle from angular momentum distributions which are snapshots of the angular momentum distribution of all particles at a given time during the collapse phase. During the collapse of a core initially in either solid-body rotation or differential rotation, particles conserve their specific angular momentum during the accretion on the stellar embryo (Cassen & Moosman 1981; Terebey et al. 1984; Goodwin et al. 2004). In the case of a protostellar envelope with a density profile $\rho \propto r^{-2}$, an observed flat profile $j(r)$ = constant requires, since each particle at different radii has the same specific angular momentum, an initially uniform distribution of angular momentum. This does not agree with the steep increase in specific angular momentum we observe at scales of $r > 1600$ au in the $j(r)$ profiles. The break in the specific angular momentum profile could be due either to a faster collapse of the inner envelope caused by an initial inner density plateau (Takahashi et al. 2016) or to a change of dominant mechanisms responsible for the observed velocity gradients from inner to outer scales of the envelope.

In our sample, we distinguish eight sources with a relatively flat $j(r)$ profile in the inner envelope ($\beta < 0.5$, see Table F.1): L1448-2A, L1448-NB, L1448-C, IRAS2A, SVS13-B, IRAS4B, L1527, and GF9-2. We estimate a centrifugal radius that would be obtained when the mass currently observed at ∼100 au collapses and based on the mean value of specific angular momentum observed today $\langle j_{100\ \rm au}\rangle$ as follows:

$$R_{\rm cent} = \frac{\langle j_{100\ \rm au}\rangle^2}{G\, M_{100\ \rm au}}. \qquad (2)$$

Table 4. Centrifugal radius $R_{\rm cent}$ assuming angular momentum conservation.

Source	$\langle j_{100\ \rm au}\rangle^{(a)}$ (10^{-4} km s^{-1} pc)	$M_{100\ \rm au}{}^{(b)}$ ($M_\odot$)	$R_{\rm cent}{}^{(c)}$ (au)	$R^{\rm dust}_{\rm disk}{}^{(d)}$ (au)	$M^{\rm min}_{100\ \rm au}{}^{(e)}$ ($M_\odot$)
L1448-2A	4.5 ± 0.2	0.005–0.2	50–1810	<50	0.2
L1448-NB	16.0 ± 0.4	0.042–0.2	500–2920	<50	3.0
L1448-C	6.0 ± 0.2	0.025–0.2	70–690	41 ± 15	0.5
IRAS2A	3.8 ± 0.4	0.020–0.2	30–330	$\lesssim 65$	0.1
SVS13-B	2.5 ± 0.2	0.019–0.2	10–160	$\lesssim 75$	0.05
IRAS4B	2.5 ± 0.3	0.003–0.2	10–840	155 ± 30	0.02
L1527	5.6 ± 0.1	0.001–0.2	70–1060	54 ± 10	0.3
GF9-2	3.9 ± 0.3	0.002–0.2	40–3080	36 ± 9	0.2

Notes. [a]Weighted mean of specific angular momentum in the inner envelopes (50 au $< r \leq$ 1600 au). [b]Range of the object mass at 100 au, the minimum and maximum values are defined in Sect. 5.3. [c]Centrifugal radii estimated from $\langle j_{100\ \rm au}\rangle$ and $M_{100\ \rm au}$ using Eq. (2), assuming conservation of angular momentum. [d]Candidate disk radius determined from the CALYPSO study of PdBI dust continuum emission at 1.3 and 3 mm (Maury et al. 2019), corrected by the assumed distance (see Table 1). [e]Total minimum mass that needs to be enclosed at $r < 100$ au to form a disk equal to $R^{\rm dust}_{\rm disk}$ if the angular momentum $\langle j_{100\ \rm au}\rangle$ was conserved. This minimum mass considers the mass of the stellar embryo and the mass of the optically thick inner envelope enclosed within 100 au.

The lower limit of the mass enclosed within 100 au, $M_{100\ \rm au}$, is the mass of the envelope $M^{\rm dust}_{100\ \rm au}$ estimated from the PdBI 1.3 mm dust continuum flux (Maury et al. 2019), assuming optically thin emission, a dust temperature at 100 au computed with Eq. (D.2) and corrected by the assumed distance (see Table 1). This mass estimate does not include the mass of the central stellar object, $M_\star$: since the embryo mass is unknown for most sources in our sample, we consider an upper limit of $M_{100\ \rm au} = M_\star + M^{\rm dust}_{100\ \rm au}$ assuming $M_\star = 0.2\ M_\odot$ for each source in our sample. This value of 0.2 $M_\odot$ corresponds to the stellar mass in the Class 0/I protostar L1527 from kinematic models of the Keplerian pattern in the disk (Tobin et al. 2012; Ohashi et al. 2014; Aso et al. 2017). The range of values for $M_{100\ \rm au}$ are reported in the third column in Table 4. The calculated range of centrifugal radii associated with $M_{100\ \rm au}$ is listed for each source in the fourth column in Table 4. We note that if $M_\star$ of a source is smaller than that of L1527, then the centrifugal radius value we calculated is underestimated.

Since the embryo mass is uncertain and $M_{100\ \rm au}$ may be underestimated if the dust emission is not optically thin, we compute the mass enclosed within $r < 100$ au, including the stellar embryo mass, needed to form a disk the size of $R^{\rm dust}_{\rm disk}$ with the $\langle j_{100\ \rm au}\rangle$ observed. The values are reported in the last column of Table 4.

For all the sources in our sample, the upper limits of the $R_{\rm cent}$ range are larger than 150 au and systematically larger than the continuum disk candidate radii $R^{\rm dust}_{\rm disk}$ from Maury et al. (2019) reported in the fifth column of Table 4. Moreover, Maret et al. (2020) only detect possible Keplerian rotation in two protostars in our sample (L1527 at radii ~90 au and L1448-C at $r \sim 200$ au) from the CALYPSO data. Thus, most $R_{\rm cent}$ values is expected to be less than 100 au. The upper $R_{\rm cent}$ values are probably overestimated because the contribution of the embryo mass to $M_{100\ \rm au}$ is excluded.

Comparing the lower limits of the $R_{\rm cent}$ range with the candidate disk radius, we find a good agreement for most sources in our sample except for L1448-NB. We find a larger centrifugal radius (~500 au) than the observed disk size (<50 au) calculated considering only the main protostar L1448-NB1 of the binary system. Since in this study, we are interested in the kinematics of the whole system, we must consider all the continuum structure and not only that of the main protostar. Considering NB1 and NB2, Maury et al. (2019) resolve a circumbinary structure with a radius of (320 ± 90) au centered on the middle of the two components. Given the uncertainties, the latter value is consistent with the lower centrifugal radius estimated here. At these scales, Tobin et al. (2016a) observe a spiral structure surrounding the multiple system and interpreted it as a gravitationally unstable circumbinary disk. On the other hand, Maury et al. (2019) suggest that this component is due to orbital motions and tidal arms between the companions and Maret et al. (2020) do not detect any Keplerian rotation at radii <170 au. Thus, the nature of this additional structure surrounding the multiple system is still unclear. As a consequence, the increase in specific angular momentum we measured at small scales could not only trace the rotation of the disk or the envelope but may be contaminated by gravitational instabilities due to orbital motions or a fragmented disk surrounding the system. Given the large uncertainties on the dust disk radii, we found a good agreement between centrifugal radii and $R^{\rm dust}_{\rm disk}$ for L1448-C and L1527. Moreover, the dust radius (50 au in L1527, Maury et al. 2019) does not necessarily exactly correspond to the centrifugal radius which was first detected in L1527 from observations of SO emission at 100 ± 20 au (Sakai et al. 2014). For this source, our estimate of $R_{\rm cent}$ (~70 au) is consistent with previous kinematic studies which detect a protoplanetary disk candidate with a radius of 50−90 au (Ohashi et al. 2014; Aso et al. 2017; Maret et al. 2020). Moreover, we observe a slight increase in the specific angular momentum we measured at $r < 80$ au. It could be due to the transition from the envelope to the disk.

The hypothesis of collapsing material with conservation of angular momentum, resulting in disk formation, at $r < 100$ au is therefore plausible for most sources in our sample. We notice that L1448-NB, in which Tobin et al. (2016a) claim the detection of a large candidate disk, shows the highest value of specific angular momentum at $r < 1600$ au of the CALYPSO sample, consistent with the angular momentum observed in the proto-planetary disks surrounding the T-Tauri stars which are estimated to be $1{-}6{\times}10^{-3}$ km s^{-1} pc (Simon et al. 2000; Kurtovic et al. 2018; Pérez et al. 2018). It could suggest an increase in the angular momentum of the disk during its evolution. In this case, the mean value of $j(r)$ in the inner envelope would be lower in the less evolved than in the more evolved Class 0 protostars, and it would increase with time until reaching the value contained in the T-Tauri disks. In this scenario, L1448-NB would be one of the most evolved objects in the sample. However, the borderline Class 0/I protostar L1527, which is the most evolved object of the CALYPSO sample, has a specific angular momentum of ~6 $\times 10^{-4}$ km s^{-1} pc at the inner envelope scales (see Table 4). In the same way, L1448-C has a specific angular momentum less than one order of magnitude lower than the values observed in the Class II disks while Maret et al. (2020) suggest the presence of a Keplerian disk in the inner envelope. As most of the CALYPSO inner protostellar envelopes have an order of magnitude less specific angular momentum than in Class II disks, we discuss below several possible explanations:

(i) a part of the angular momentum inherited by the T-Tauri disks may not come from the rotating matter contained in the inner envelope accreted during the Class 0 phase. During the Class I phase, the mass accreted could come from regions further away from the envelope ($r \gg 1600$ au) with a possibly higher specific angular momentum;

(ii) disks may expand with time due to the transfer of angular momentum from their inner regions to their outer ones. Unfortunately, the specific angular momentum does not contain information about the mass. Large values of $j(r)$ may be carried by low masses at the outer disk radius but may remain difficult to quantify. To this day, the mechanisms at work in disk evolution remain an open question. Some studies, for example, suggest that viscous friction may be responsible for the disk expansion (Najita & Bergin 2018);

(iii) the specific angular momentum of the proto-planetary disks may be biased toward high values from historical, large and massive disks. A new population of small T-Tauri disks with radii between 10 and 30 au has been observed thanks to PdBI and ALMA (Piétu et al. 2014; Cieza et al. 2019). Assuming a small rotationally-supported disks around a stellar object including a total mass of 0.1−1 $M_{\odot}$ (Piétu et al. 2014), one expects a specific angular momentum between 10^{-5} and 10^{-4} km s^{-1} pc, values which are similar to those we obtained in the inner Class 0 protostellar envelopes with the CALYPSO sample. However, to this day, no resolved observations of gas kinemactics of these small Class II disks allow us to estimate observationally their specific angular momentum.

5.4. Origin of the velocity gradients at $r > 1600$ au

At outer envelope scales, we detect velocity gradients (~2 km s^{-1} pc^{-1} at ~10 000 au, see Table 2) in the CALYPSO single-dish maps. They may not be directly related to rotational motions of the envelopes but rather to other mechanisms. Indeed, we observe in the CALYPSO dataset a systematic evolution of the orientation of the gradients between the inner and outer scales in the envelope (see Table 2). Figure 19 shows the orientation of the mean velocity gradient observed at different scales of the envelope with respect to the position angle of the gradient observed at scales ~100 au. The clear dispersion (~100° on average, see Fig. 19) of gradient position angle across scales within individual objects may be due to a change of dominant mechanisms responsible for the observed gradients from inner to outer scales of the envelope. From the literature, velocity gradients are often measured in the outer protostellar envelopes along the equatorial axis and they are interpreted as due to rotational motions or infall from a filamentary structure at scales of 1500−10 000 au (Ohashi et al. 1997a; Belloche et al. 2002; Tobin et al. 2011). In this section, we explore the possible origins of the velocity gradients found at scales of $r > 1600$ au and used to build the $|j_{\rm app}|(r)$ profiles (see Fig. 18).

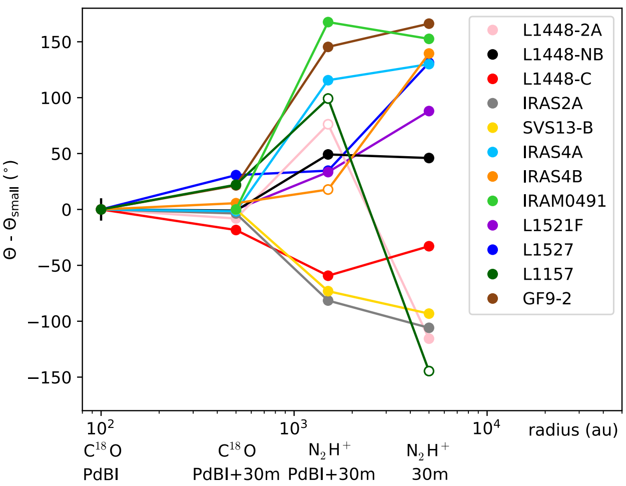

Fig. 19. Evolution of the orientation of the mean velocity gradient in the different datasets used to build the $PV_{\rm rot}$ diagrams and angular momentum distributions with respect to the PA of the velocity gradient observed at small scales $\Theta_{\rm small}$ (PdBI $C^{18}O$ emission). The error bars of the orientation Θ are given in Table 2. They are smaller than 10° except for 7 of the 67 gradient measurements. For these 7 measurements, the large error bars are generally due to the absence of a clear gradient on either side of the central position of the source. Gradient measurements with large error are indicated by an empty circle. A typical error of ±10° is shown on the first point of the plot.

5.4.1. Questioning the interpretation of counter-rotation

Six sources in the sample show a clear reversal of the orientation of the mean velocity gradient ($|\Theta - \Theta_{\rm small}| > 130°$) from the inner to the outer envelope scales: IRAS4A, IRAS4B, L1527, IRAM04191, L1157, and GF9-2. We note that the kinematics at scales where we observed reversed velocity gradients ($r > 1600$ au) with respect to the small scales were not taken into account to build the $PV_{\rm rot}$ diagrams in Fig. 16, or the specific angular momentum profiles shown for the full sample in panel b of Fig. 17. Indeed, these profiles were aimed at characterizing the rotational motions in the envelopes and the angular momentum due to this rotation: a reversal of the rotation, if real, would require a more complex model than the power-law ($\upsilon \propto r^{\alpha}$) model we adopted in Sects. 4.3–5.3. In this section, we discuss these complex patterns in more detail.

In IRAM04191, we observed velocity gradients at outer envelope scales of $r > 1600$ au consistent with those observed previously by Belloche et al. (2002) and Lee et al. (2005) ($\Theta \sim 100°$, see Table 2). However, in the inner envelope, we noticed a velocity gradient with a direction of $\Theta = -83°$ (see bottom middle panel in Fig. 10 and Table 2). In L1527, we found small-scale velocity gradients ($\Theta \sim 0°$ at $r \sim$ 1000 au) consistent with those previously observed by Tobin et al. (2011) which are in the opposite direction compared to the large-scale one ($r \sim 8000$ au, Goodman et al. 1993). Tobin et al. (2011) interpret this reversal of velocity gradients as counter-rotation but it also could be due to infalling motions that dominated the velocity field at the outer envelope scales (Harsono et al. 2014).

Our study suggests that reversals of velocity gradients are common in Class 0 protostellar envelopes. However, the asymmetrical velocity gradients (for IRAS4B, GF9-2), the filamentary structures traced by the integrated intensity at scales of $r > 2000$ au (for IRAS4A, IRAS4B, L1527, and GF9-2), and a strong external compression of the cloud hosting IRAS4A and IRAS4B (Belloche et al. 2006) lead us to exclude the observed reversed gradients as counter-rotation of the envelope. Moreover, only MHD models with Hall effect succeed to form envelopes in counter-rotation. These models form a thin layer of counter-rotating envelopes at the outer radius of the disk ($r \sim 50$–200 au; Tsukamoto et al. 2017). This envelope layer is in counter-rotation compared to the formed disk and the protostellar envelope at $r > 200$ au as a consequence of the Hall effect generated by the rotation of the disk which changes the angular momentum of the gas at the disk outer radius. Therefore, these models cannot explain the inversions of rotation in the different layers of the envelope at scales of $r > 3000$ au as observed in our sample. Historically, the gradients observed from single-dish mapping at $r > 3000$ au have been used to quantify the amplitude for the angular momentum problem. However, incorrectly interpreted as pure rotational motions in the envelope, the resulting angular momentum measurements and the expected disk radii would be significantly overestimated.

Recent studies on the angular momentum of the protostellar cores from hydrodynamical simulations of star formation are questioning the standard model of star formation from a collapsing core initially in solid-body rotation (Kuznetsova et al. 2019; Verliat et al. 2020). They show that the angular momentum of synthetic protostellar cores is not directly related to the initial rotation of the synthetic cloud, and Keplerian disks can be formed from a simple non-uniform perturbation in the initial density distribution. In this scenario, the angular momentum observed in inner protostellar envelopes and disks may not been inherited from larger-scale initial conditions but generated during the collapse itself.

5.4.2. Contribution of infalling motions and core-forming motions

The misalignments between the gradients observed in the envelopes at inner and outer envelope scales suggest a change of dominant mechanisms at $r > 1600$ au. At large scales, infalling motions of the envelope can dominate rotational motions. In the hypothesis of a flattened infalling envelope, infall motions are expected to produce a velocity gradient projected in the plane of the sky that is oriented along the minor axis of the envelope, namely at the same position angle as the outflow. In L1448-NB, SVS13-B and L1527, we detect velocity gradients aligned with the outflow axis at $r > 3000$ au while at small scales the gradients are consistent with the equatorial axis (see Table 2). These three sources could be good candidates of the transition from collapse to rotation between large and small scales. This scenario is also suggested in the study of Ohashi et al. (1997b). They suggested that at outer envelope scales of $r \sim 2000$ au, the protostellar envelope L1527 is not rotationally supported ($v_{\rm rot} \sim 0.05$ km s^{-1}) but is dominated by the collapse ($v_{\rm inf} \sim 0.3$ km s^{-1}).

Currently, there are very few constraints on the infall velocities at scales of $r > 1600$ au in the CALYPSO protostellar envelopes. Belloche et al. (2002) estimate an infall velocity of $v_{\rm inf} \sim 0.15$ km s^{-1} at $r \sim 1000$ au from radiative transfer modeling of CS and C^{34}S emission in IRAM04191. In the dense core L1544, Tafalla et al. (1998) suggest also an infall velocity of ~0.1 km s^{-1} at scales >3000 au. The velocity offset, with respect to the systemic velocity assumed for each source, found along the equatorial axis at >1000 au with CALYPSO is reported in Table 5. For most sources, we find typical velocity offsets $\lesssim$0.3 km s^{-1} at scales of 1600 au (see Table 5), consistent with infall velocities found in IRAM04191 and L1544, except for IRAS4A. IRAS4A harbors a velocity of ~0.5 km s^{-1} at $r \sim 1000$ au. This result is consistent with those of Belloche et al. (2006) at ~2000 au. They suggest that a fast collapse is triggered by an external compression from the cloud in which the source is embedded. Thus, for all sources in our sample, the velocity gradient misalignment could be due to a change of mechanism dominating the velocities projected on the line of sight. This suggests either rotational velocities much smaller than infall velocities or a non axisymmetric geometry of the kinematics at outer envelope scales.

Table 5. Value of velocity offset, with respect to the systemic velocity assumed for each source, at 100, 1000, and 10 000 au along the equatorial axis from the velocity maps and considering all the gradients observed, even those not consistent with rotational motions.

Source	$v_{100\,{\rm au}}$ (km s^{-1})	$v_{1000\,{\rm au}}$ (km s^{-1})	$v_{10000\,{\rm au}}$ (km s^{-1})
L1448-2A	0.7	0.1	1.1
L1448-NB	2.1	0.3	0.02
L1448-C	1.3	0.1	0.2
IRAS2A	0.7	0.1	0.3
SVS13-B	0.5	0.1	0.2
IRAS4A	...	0.4	0.9
IRAS4B	...	0.1	0.5
IRAM04191	0.3	0.1	0.1
L1521F	0.1	0.2	0.2
L1527	1.1	0.1	0.2
L1157	0.1	0.2	0.1
GF9-2	1.0	0.2	0.2

Moreover, *Herschel* observations have shown that most solar-type prestellar cores and protostars form in filaments (André et al. 2014). Indeed, the column density maps of the *Herschel* Gould Belt Survey program[4] (André et al. 2010) reveal that the CALYPSO protostars are embedded in or lie in the immediate vicinity of filamentary structures with $N_{\rm H_2} > 10^{21}$ cm^{-2}. Thus, the large-scale kinematics in protostellar envelopes could be contaminated or dominated by the kinematics of the filaments. Kirk et al. (2013) studied the velocity field of Serpens-South in the Aquila molecular cloud and showed a complex kinematics with longitudinal collapse along the main filament, radial contractions, and accretion streams from the cloud to the main filament. The longitudinal collapse of the filament could be responsible for the large-scale gradients observed in our protostellar envelopes as observed in the Serpens-Main region by Dhabal et al. (2018). Several studies also highlighted transverse velocity gradients perpendicular to the main filament that suggested the material may be accreting along perpendicular striations (Palmeirim et al. 2013; Dhabal et al. 2018; Arzoumanian et al. 2018; Shimajiri et al. 2019). Palmeirim et al. (2013) estimate the velocity of the infalling material to be 0.5−1 km s^{-1} at $r \sim 0.4$ pc in the B211/L1495 region. In our velocity maps at 10 000 au along the equatorial axis, we measure typical velocities <0.3 km s^{-1} in most of the sources (see Table 5) except in L1448-2A, IRAS4A, and IRAS4B. These three sources

---

[4] See `http://gouldbelt-herschel.cea.fr/archives`

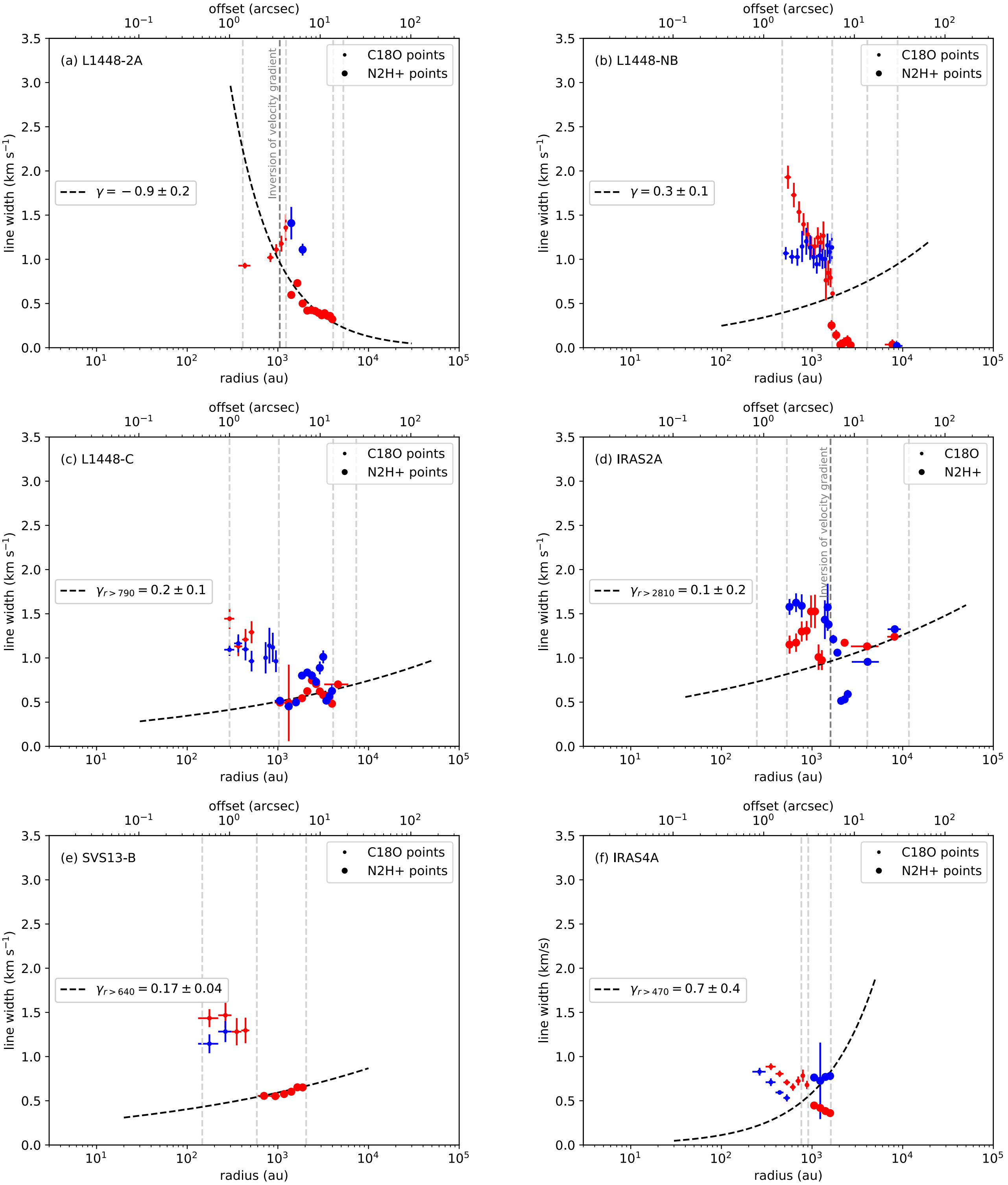

Fig. 20. Linewidth along the equatorial axis of the CALYPSO protostellar envelopes. Blue and red dots show the linewidths at positions that have blue- and red-shifted velocities, respectively. Dots and large dots show the $C^{18}O$ and N_2H^+ data, respectively. The dashed curve shows the best fit with a power-law model leaving the index γ as a free parameter ($Dv \propto r^{\gamma}$) in the outer envelope (see Appendix G). The radius of the outer envelope is given by the break radius of the $j(r)$ or $j_{\rm app}(r)$ profiles (see Tables F.1 and F.2) or the radius where we observe a reversal of the velocity gradients with respect to the inner envelope. The vertical dashed lines show the transition radii between the different datasets (PdBI, combined, and 30m) and the two tracers as given in Table C.1.

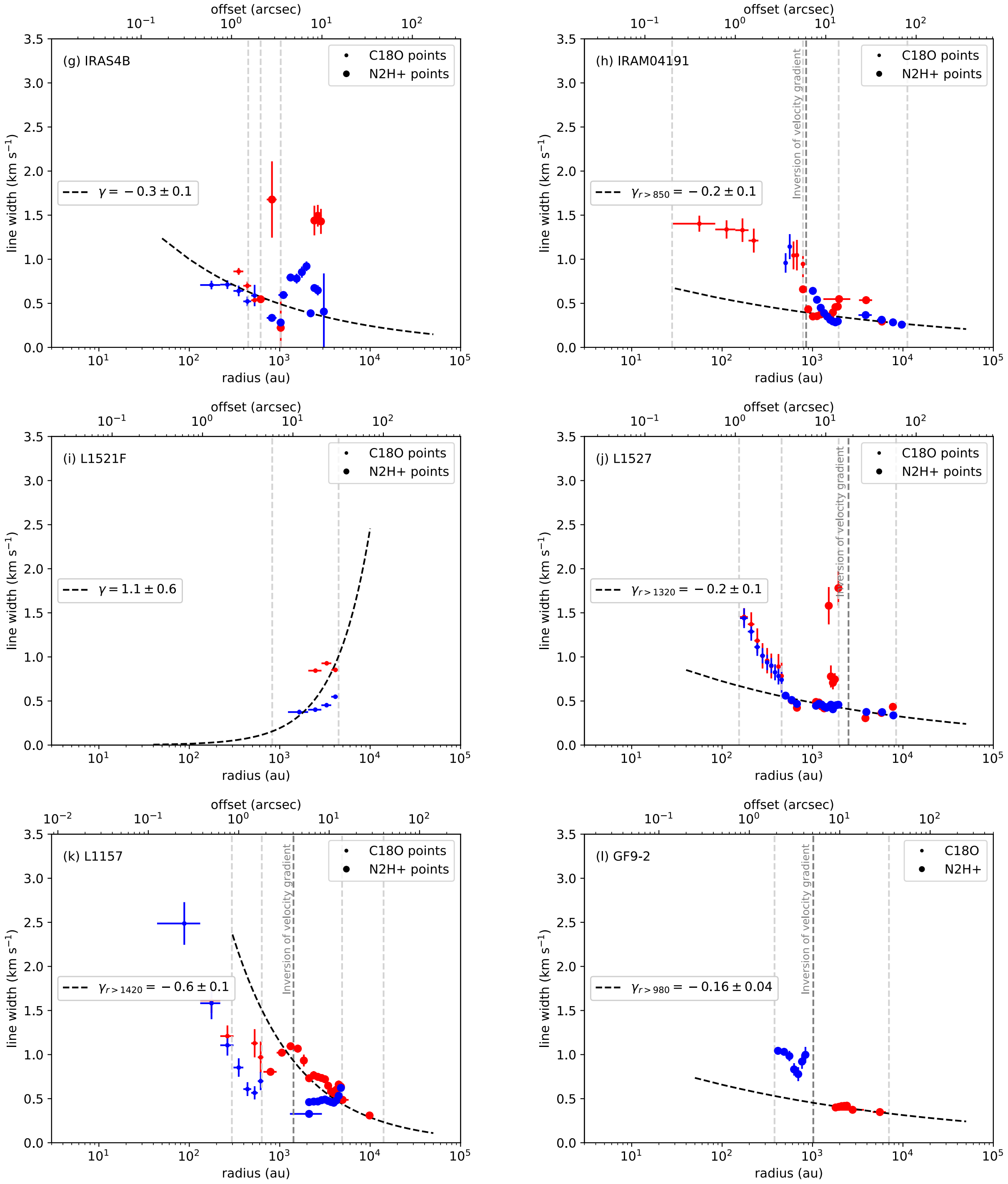

Fig. 20. continued.

exhibit velocities of 0.5–1 km s^{-1} consistent with infall velocities estimated at filamentary scales. In these cases, host-filament motions could dominate the kinematics in outer protostellar envelopes ($r > 1600$ au).

5.4.3. Contamination by turbulent motions from cloud scales

All sources of the CALYPSO subsample (except L1448-NB) reveal a steep increase in apparent specific angular momentum with the radius at ~1600–10000 au scales, with an average trend of $j_{\rm app} \propto r^{1.6\pm0.2}$ (see Table F.2 and Fig. 18). This trend is similar to that observed in prestellar cores and clumps at scales >10 000 au (see Figs. 17 and 18). Indeed, Goodman et al. (1993), Caselli et al. (2002) and Tatematsu et al. (2016) show a trend between the size of prestellar cores and their observed mean angular momenta at scales on the order of 0.1 pc: $j(r)$ distribution scaling as $r^{1.2-1.7}$. From this dependency of j with core radius and the linewidth-size relation, Tatematsu et al. (2016)

suggest that non-thermal motions (turbulence) are related to the origin of angular momentum observed in these 0.1 pc cores.

Burkert & Bodenheimer (2000) studied numerical models of turbulent molecular clouds with a symmetric density profile and a Gaussian or random velocity field. They showed that 0.1 pc cores with random motions exhibit most of the time velocity gradients that, interpreted as rotation, would have specific angular momentum values of $j \sim 3 \times 10^{-3}$ km s^{-1} pc (10^{21} cm^2 s^{-1}) and would scale as $j \propto r^{1.5}$. This is in good agreement with observed values at 0.1 pc from the literature (Goodman et al. 1993; Caselli et al. 2002; Tatematsu et al. 2016). Our observations showing a trend of $j \propto r^{1.6}$ at scales ~1600–5000 au could be either a signature of the turbulent cascade from the large-scale ISM propagating with subsonic properties to 1600 au envelope scales, or gravitationally-driven turbulence due to large-scale collapse motions at the interface between filaments and cores (Kirk et al. 2013).

From the analysis of the gas velocity dispersion in molecular line observations, Goodman et al. (1998) and Pineda et al. (2010) identify the dense cores at a typical scale of 0.1 pc as the first velocity-coherent structures decoupled from the turbulent cloud. In this case, we would expect a quiescent structure with subsonic motions at radii <0.1 pc and the interpretation of ISM turbulent cascade with supersonic motions as a consequence of the steep increase of $j_{\rm app}$ at scales <10 000 au would no longer be valid. Except L1448-2A, IRAS4A, and IRAS4B which exhibit velocities 0.5−1 km s^{-1} consistent with supersonic turbulent motions, all sources in our sample show typical velocities $\lesssim$0.3 km s^{-1} consistent with subsonic-transonic turbulent motions. This could suggest that the power-law behavior of $j_{\rm app} \propto r^{1.6}$ observed in the outer envelopes ($r > 1600$ au) could be a scaling law due to the tail of a low velocity subsonic-transonic turbulent cascade.

At scales of $r > 1600$ au, we observe typical velocity linewidths $\lesssim$1 km s^{-1} (see Fig. 20). We note that the linewidths tend to decrease from ~1600 au to larger scales in the outer envelopes and they do not show scaling laws with the radius as expected from turbulent motions in the ISM (Larson 1981; see Fig. 20 and Table G.1), but the velocity structure at these scales seems to show multiple components in velocity for several sources (L1527, L1448-C, IRAS2A, SVS13-B, IRAS4A, IRAS4B). As we can not disentangle them and identify exactly which component comes from the outer envelope or the host cloud for example, we need either a more elaborate model than a Gaussian or a HFS model to analyze the spectra or a more suitable tracer to determine more robustly the linewidths of the outer envelopes.

6. Conclusions

In the framework of the CALYPSO survey, we analyzed the kinematics of Class 0 protostellar envelopes. The main results of our study are listed below.

1. We identify differential rotation motions in 11 sources in a sample of 12 Class 0 protostellar envelopes. The only exception is IRAS4A: the motions reported in the PV$_{\rm rot}$ and modeled by a power-law function are consistent with a solid-body rotation, but the velocity gradient is not uniform in the inner envelope at $r < 2000$ au as would be expected.
2. This is the first time that the specific angular momentum distribution as a function of envelope radius is determined homogeneously for a large sample of 11 Class 0 protostars. The high angular resolution and the high dynamic range of the CALYPSO observations allow us to identify two distinct regimes: the apparent specific angular momentum decreases as $j_{\rm app} \propto r^{1.6\pm0.2}$ down to ~1600 au and then tends to become relatively constant around ~6 × 10^{-4} km s^{-1} pc down to ~50 au.
3. The values of specific angular momentum measured in the inner Class 0 envelopes suggest that material directly involved in the star formation process (<1600 au) typically encloses the same order of magnitude in specific angular momentum as what is inferred in small T-Tauri disks ($r \sim 10$ au). The constant values of j at 50−1600 au allow us to determine good estimates of the centrifugal radius in the Class 0 protostars of the CALYPSO sample, which compare well with the disk radii estimated from the dust continuum (Maury et al. 2019). This suggests that the specific angular momentum is conserved during the accretion on the stellar embryo, resulting in disk formation.
4. At scales of $r > 1600$ au, we conclude that the velocity gradients observed in the outer envelope with respect to small scales are not due to pure rotational motions or counter-rotation motions but related to other mechanisms. Historically, the gradients observed from single-dish mapping at $r > 3000$ au have been interpreted as rotation and used to quantify the amplitude of the angular momentum problem for star formation. Thus, if the gradients are incorrectly interpreted as rotation, the angular momentum problem for star formation and the expected disk radii may have been significantly over-estimated. Moreover, we find no robust hints that envelopes are rotating with typical velocities higher than the sound speed at scales of $r > 1600$ au. This suggests that the origin of angular momentum in the outer protostellar envelopes could be the gravitationally-driven turbulence due to large-scale collapse motions at the interface between filaments and cores, or the dissipation of the large-scale ISM turbulent cascade propagating with subsonic velocities to 1600 au envelope scales.

Acknowledgements. We thank the IRAM staff for their support carrying out the CALYPSO observations. This work has benefited from the support of the European Research Council under the European Union's Seventh Framework Programme (Advanced Grant ORISTARS with grant agreement no. 291294 and Starting Grant MagneticYSOs with grant agreement no. 679937). M.G. thanks the Max-Planck Institute for Radio Astronomy for its support toward the end of this work. We would like to thank Cecilia Cecarelli for comments and suggestions on the estimation of column density, and Nagayoshi Ohashi and Jaime E. Pineda for valuable discussions on the interpretation. We also thank the referee for the useful comments which helps to improve this paper.

References

Anderl, S., Maret, S., Cabrit, S., et al. 2016, A&A, 591, A3
Anderl, S., Maret, S., Cabrit, S., et al. 2020, A&A, submitted
André, P., Ward-Thompson, D., & Barsony, M. 1993, ApJ, 406, 122
André, P., Motte, F., & Bacmann, A. 1999, ApJ, 513, L57
André, P., Ward-Thompson, D., & Barsony, M. 2000, Protostars and Planets IV (Tucson, AZ: University of Arizona Press), 59
André, P., Men'shchikov, A., Bontemps, S., et al. 2010, A&A, 518, L102
André, P., Di Francesco, J., Ward-Thompson, D., et al. 2014, Protostars and Planets VI, eds. H. Beuther, R. S. Klessen, C. P. Dullemond, & T. Henning (Tucson, AZ: University of Arizona Press), 27
Andrews, S. M., Wilner, D. J., Hughes, A. M., Qi, C., & Dullemond, C. P. 2009, ApJ, 700, 1502
Anglada, G., Rodriguez, L. F., Torrelles, J. M., et al. 1989, ApJ, 341, 208
Arzoumanian, D., Shimajiri, Y., Inutsuka, S.-i., Inoue, T., & Tachihara, K. 2018, PASJ, 70, 96
Aso, Y., Ohashi, N., Aikawa, Y., et al. 2017, ApJ, 849, 56
Bachiller, R., & Pérez Gutiérrez, M. 1997, ApJ, 487, L93
Bachiller, R., Cernicharo, J., Martin-Pintado, J., Tafalla, M., & Lazareff, B. 1990, A&A, 231, 174
Bachiller, R., Andre, P., & Cabrit, S. 1991, A&A, 241, L43

Bachiller, R., Guilloteau, S., Dutrey, A., Planesas, P., & Martin-Pintado, J. 1995, A&A, 299, 857

Bachiller, R., Guilloteau, S., Gueth, F., et al. 1998, A&A, 339, L49

Bachiller, R., Gueth, F., Guilloteau, S., Tafalla, M., & Dutrey, A. 2000, A&A, 362, L33

Bachiller, R., Pérez Gutiérrez, M., Kumar, M. S. N., & Tafalla, M. 2001, A&A, 372, 899

Barsony, M., Ward-Thompson, D., André, P., & O'Linger, J. 1998, ApJ, 509, 733

Basu, S. 1998, ApJ, 509, 229

Belloche, A. 2013, EAS Pub. Ser., 62, 25

Belloche, A., & André, P. 2004, A&A, 419, L35

Belloche, A., André, P., Despois, D., & Blinder, S. 2002, A&A, 393, 927

Belloche, A., Hennebelle, P., & André, P. 2006, A&A, 453, 145

Belloche, A., Maury, A. J., Maret, S., et al. 2020, A&A, in press, `https://doi.org/10.1051/0004-6361/201937352`

Beltrán, M. T., Gueth, F., Guilloteau, S., & Dutrey, A. 2004, A&A, 416, 631

Benson, P. J., & Myers, P. C. 1989, ApJS, 71, 89

Bergin, E. A., Alves, J., Huard, T., & Lada, C. J. 2002, ApJ, 570, L101

Blandford, R. D., & Payne, D. G. 1982, MNRAS, 199, 883

Bodenheimer, P. 1995, ARA&A, 33, 199

Bourke, T. L., Myers, P. C., Evans, N. J., I, et al. 2006, ApJ, 649, L37

Bouvier, J., Cabrit, S., Fernandez, M., Martin, E. L., & Matthews, J. M. 1993, A&A, 272, 176

Brinch, C., Jørgensen, J. K., & Hogerheijde, M. R. 2009, A&A, 502, 199

Burkert, A., & Bodenheimer, P. 2000, ApJ, 543, 822

Carter, M., Lazareff, B., Maier, D., et al. 2012, A&A, 538, A89

Caselli, P., Myers, P. C., & Thaddeus, P. 1995, ApJ, 455, L77

Caselli, P., Benson, P. J., Myers, P. C., & Tafalla, M. 2002, ApJ, 572, 238

Cassen, P., & Moosman, A. 1981, Icarus, 48, 353

Ceccarelli, C., Hollenbach, D. J., & Tielens, A. G. G. M. 1996, ApJ, 471, 400

Chandler, C. J., & Richer, J. S. 2000, ApJ, 530, 851

Chen, X., Launhardt, R., & Henning, T. 2007, ApJ, 669, 1058

Chen, X., Launhardt, R., & Henning, T. 2009, ApJ, 691, 1729

Chiang, H.-F., Looney, L. W., Tobin, J. J., & Hartmann, L. 2010, ApJ, 709, 470

Ching, T.-C., Lai, S.-P., Zhang, Q., et al. 2016, ApJ, 819, 159

Chini, R., Reipurth, B., Sievers, A., et al. 1997, A&A, 325, 542

Choi, M. 2001, ApJ, 553, 219

Ciardi, D. R., Woodward, C. E., Clemens, D. P., Harker, D. E., & Rudy, R. J. 2000, AJ, 120, 393

Cieza, L. A., Ruíz-Rodríguez, D., Hales, A., et al. 2019, MNRAS, 482, 698

Codella, C., Lorenzani, A., Gallego, A. T., Cesaroni, R., & Moscadelli, L. 2004, A&A, 417, 615

Codella, C., Welser, R., Henkel, C., Benson, P. J., & Myers, P. C. 1997, A&A, 324, 203

Codella, C., Cabrit, S., Gueth, F., et al. 2014a, A&A, 568, L5

Codella, C., Maury, A. J., Gueth, F., et al. 2014b, A&A, 563, L3

Crapsi, A., Caselli, P., Walmsley, C. M., et al. 2004, A&A, 420, 957

Curiel, S., Raymond, J. C., Rodriguez, L. F., Canto, J., & Moran, J. M. 1990, ApJ, 365, L85

Curiel, S., Torrelles, J. M., Rodríguez, L. F., Gómez, J. F., & Anglada, G. 1999, ApJ, 527, 310

Daniel, F., Dubernet, M. L., Meuwly, M., Cernicharo, J., & Pagani, L. 2005, MNRAS, 363, 1083

De Simone, M., Codella, C., Testi, L., et al. 2017, A&A, 599, A121

Desmurs, J.-F., Codella, C., Santiago-García, J., Tafalla, M., & Bachiller, R. 2009, A&A, 498, 753

Dhabal, A., Mundy, L. G., Rizzo, M. J., Storm, S., & Teuben, P. 2018, ApJ, 853, 169

di Francesco, J., Evans, N. J., I., Caselli, P., et al. 2007, in Protostars and Planets V, eds. B. Reipurth, D. Jewitt, & K. Keil (Tucson, AZ: University of Arizona Press), 17

Dunham, M. M., Evans, N. J., I, Bourke, T. L., et al. 2006, ApJ, 651, 945

Endres, C. P., Schlemmer, S., Schilke, P., Stutzki, J., & Müller, H. S. P. 2016, J. Mol. Spectr., 327, 95

Enoch, M. L., Evans, N J., I, Sargent, A. I., & Glenn, J. 2009, ApJ, 692, 973

Evans, N. J., I, Dunham, M. M., Jørgensen, J. K., et al. 2009, ApJS, 181, 321

Flower, D. R. 2001, MNRAS, 328, 147

Furuya, R. S., Kitamura, Y., & Shinnaga, H. 2006, ApJ, 653, 1369

Girart, J. M., & Acord, J. M. P. 2001, ApJ, 552, L63

Girart, J. M., Rao, R., & Marrone, D. P. 2006, Science, 313, 812

Goldsmith, P. F., & Arquilla, R. 1985, in Protostars and Planets II, eds. D. C. Black & M. S. Matthews (Tucson, AZ: University of Arizona Press), 137

Goldsmith, P. F., & Langer, W. D. 1999, ApJ, 517, 209

Goodman, A. A., Benson, P. J., Fuller, G. A., & Myers, P. C. 1993, ApJ, 406, 528

Goodman, A. A., Barranco, J. A., Wilner, D. J., & Heyer, M. H. 1998, ApJ, 504, 223

Goodwin, S. P., Whitworth, A. P., & Ward-Thompson, D. 2004, A&A, 414, 633

Grossman, E. N., Masson, C. R., Sargent, A. I., et al. 1987, ApJ, 320, 356

Gueth, F., Guilloteau, S., & Bachiller, R. 1996, A&A, 307, 891

Gueth, F., Bachiller, R., & Tafalla, M. 2003, A&A, 401, L5

Guilloteau, S., Bachiller, R., Fuente, A., & Lucas, R. 1992, A&A, 265, L49

Harsono, D., Jørgensen, J. K., van Dishoeck, E. F., et al. 2014, A&A, 562, A77

Hartmann, L., Calvet, N., Gullbring, E., & D'Alessio, P. 1998, ApJ, 495, 385

Hirano, N., Ho, P. P. T., Liu, S.-Y., et al. 2010, ApJ, 717, 58

Hirota, T., Honma, M., Imai, H., et al. 2011, PASJ, 63, 1

Hull, C. L. H., Plambeck, R. L., Kwon, W., et al. 2014, ApJS, 213, 13

Isella, A., Carpenter, J. M., & Sargent, A. I. 2009, ApJ, 701, 260

Jennings, R. E., Cameron, D. H. M., Cudlip, W., & Hirst, C. J. 1987, MNRAS, 226, 461

Jørgensen, J. K., & van Dishoeck, E. F. 2010, ApJ, 710, L72

Jørgensen, J. K., Hogerheijde, M. R., van Dishoeck, E. F., Blake, G. A., & Schöier, F. L. 2004, A&A, 413, 993

Jørgensen, J. K., Bourke, T. L., Myers, P. C., et al. 2007, ApJ, 659, 479

Karska, A., Herczeg, G. J., van Dishoeck, E. F., et al. 2013, A&A, 552, A141

Kirk, H., Myers, P. C., Bourke, T. L., et al. 2013, ApJ, 766, 115

Knee, L. B. G., & Sandell, G. 2000, A&A, 361, 671

Kurono, Y., Saito, M., Kamazaki, T., Morita, K.-I., & Kawabe, R. 2013, ApJ, 765, 85

Kurtovic, N. T., Pérez, L. M., Benisty, M., et al. 2018, ApJ, 869, L44

Kuznetsova, A., Hartmann, L., & Heitsch, F. 2019, ApJ, 876, 33

Kwon, W., Looney, L. W., Crutcher, R. M., & Kirk, J. M. 2006, ApJ, 653, 1358

Ladd, E. F., Adams, F. C., Casey, S., et al. 1991, ApJ, 382, 555

Larson, R. B. 1981, MNRAS, 194, 809

Lay, O. P., Carlstrom, J. E., & Hills, R. E. 1995, ApJ, 452, L73

Lee, C.-F., Ho, P. T. P., & White, S. M. 2005, ApJ, 619, 948

Lee, K. I., Dunham, M. M., Myers, P. C., et al. 2015, ApJ, 814, 114

Lefèvre, C., Cabrit, S., Maury, A. J., et al. 2017, A&A, 604, L1

Looney, L. W., Mundy, L. G., & Welch, W. J. 2000, ApJ, 529, 477

Looney, L. W., Mundy, L. G., & Welch, W. J. 2003, ApJ, 592, 255

Looney, L. W., Tobin, J. J., & Kwon, W. 2007, ApJ, 670, L131

López-Sepulcre, A., Sakai, N., Neri, R., et al. 2017, A&A, 606, A121

Lynden-Bell, D., & Pringle, J. E. 1974, MNRAS, 168, 603

Machida, M. N., Inutsuka, S.-i., & Matsumoto, T. 2014, MNRAS, 438, 2278

Mangum, J. G., & Shirley, Y. L. 2015, PASP, 127, 266

Maret, S., Bergin, E. A., & Lada, C. J. 2007, ApJ, 670, L25

Maret, S., Belloche, A., Maury, A. J., et al. 2014, A&A, 563, L1

Maret, S., Ceccarelli, C., Caux, E., Tielens, A. G. G. M., & Castets, A. 2002, A&A, 395, 573

Maret, S., Maury, A. J., Belloche, A., et al. 2020, A&A, 635, A15

Masson, J., Chabrier, G., Hennebelle, P., Vaytet, N., & Commerçon, B. 2016, A&A, 587, A32

Mather, J. C., Cheng, E. S., Cottingham, D. A., et al. 1994, ApJ, 420, 439

Maury, A. J., André, P., Hennebelle, P., et al. 2010, A&A, 512, A40

Maury, A. J., André, P., Men'shchikov, A., Könyves, V., & Bontemps, S. 2011, A&A, 535, A77

Maury, A. J., Belloche, A., André, P., et al. 2014, A&A, 563, L2

Maury, A. J., André, P., Testi, L., et al. 2019, A&A, 621, A76

Mizuno, A., Onishi, T., Hayashi, M., et al. 1994, Nature, 368, 719

Motte, F., & André, P. 2001, A&A, 365, 440

Najita, J. R., & Bergin, E. A. 2018, ApJ, 864, 168

Ohashi, N., Hayashi, M., Ho, P. T. P., et al. 1997a, ApJ, 488, 317

Ohashi, N., Hayashi, M., Ho, P. T. P., & Momose, M. 1997b, ApJ, 475, 211

Ohashi, N., Lee, S., Wilner, D., & Hayashi, M. 1999, ApJ, 518, L41

Ohashi, N., Saigo, K., Aso, Y., et al. 2014, ApJ, 796, 131

O'Linger, J., Wolf-Chase, G., Barsony, M., & Ward-Thompson, D. 1999, ApJ, 515, 696

Onishi, T., Mizuno, A., & Fukui, Y. 1999, PASJ, 51, 257

Ortiz-León, G. N., Loinard, L., Dzib, S. A., et al. 2018, ApJ, 869, L33

Palmeirim, P., André, P., Kirk, J., et al. 2013, A&A, 550, A38

Pelletier, G., & Pudritz, R. E. 1992, ApJ, 394, 117

Pérez, L. M., Benisty, M., Andrews, S. M., et al. 2018, ApJ, 869, L50

Pety, J. 2005, in SF2A-2005: Semaine de l'Astrophysique Francaise, eds. F. Casoli, T. Contini, J. M. Hameury, & L. Pagani, 721

Piétu, V., Guilloteau, S., Di Folco, E., Dutrey, A., & Boehler, Y. 2014, A&A, 564, A95

Pineda, J. E., Goodman, A. A., Arce, H. G., et al. 2010, ApJ, 712, L116

Pineda, J. E., Zhao, B., Schmiedeke, A., et al. 2019, ApJ, 882, 103

Plunkett, A. L., Arce, H. G., Corder, S. A., et al. 2013, ApJ, 774, 22

Podio, L., Codella, C., Gueth, F., et al. 2016, A&A, 593, L4
Pudritz, R. E., Ouyed, R., Fendt, C., & Brandenburg, A. 2007, in Protostars and Planets V, eds. B. Reipurth, D. Jewitt, & K. Keil (Tucson, AZ: University of Arizona Press), 277
Redman, M. P., Keto, E., Rawlings, J. M. C., & Williams, D. A. 2004, MNRAS, 352, 1365
Reid, M. J., Dame, T. M., Menten, K. M., & Brunthaler, A. 2016, ApJ, 823, 77
Ricci, L., Testi, L., Natta, A., et al. 2010, A&A, 512, A15
Sadavoy, S. I., Di Francesco, J., André, P., et al. 2014, ApJ, 787, L18
Sakai, N., Sakai, T., Hirota, T., et al. 2014, Nature, 507, 78
Sandell, G., & Knee, L. 2001, in Science with the Atacama Large Millimeter Array, ed. A. Wootten (San Francisco: ASP), 235, 154
Sandell, G., Knee, L. B. G., Aspin, C., Robson, I. E., & Russell, A. P. G. 1994, A&A, 285, L1
Santangelo, G., Codella, C., Cabrit, S., et al. 2015, A&A, 584, A126
Schneider, S., & Elmegreen, B. G. 1979, ApJS, 41, 87
Segura-Cox, D. M., Harris, R. J., Tobin, J. J., et al. 2016, ApJ, 817, L14
Shimajiri, Y., André, P., Palmeirim, P., et al. 2019, A&A, 623, A16
Shu, F. H. 1977, ApJ, 214, 488
Simon, M., Dutrey, A., & Guilloteau, S. 2000, ApJ, 545, 1034
Spezzi, L., Cox, N. L. J., Prusti, T., et al. 2013, A&A, 555, A71
Tafalla, M., & Bachiller, R. 1995, ApJ, 443, L37
Tafalla, M., Mardones, D., Myers, P. C., et al. 1998, ApJ, 504, 900
Takahashi, S. Z., Tomida, K., Machida, M. N., & Inutsuka, S.-i. 2016, MNRAS, 463, 1390
Takakuwa, S., Ohashi, N., & Hirano, N. 2003, ApJ, 590, 932
Tatematsu, K., Ohashi, S., Sanhueza, P., et al. 2016, PASJ, 68, 24
Terebey, S., Shu, F. H., & Cassen, P. 1984, ApJ, 286, 529
Terebey, S., Chandler, C. J., & Andre, P. 1993, ApJ, 414, 759
Terebey, S., Fich, M., Noriega-Crespo, A., et al. 2009, ApJ, 696, 1918
Tobin, J. J., Looney, L. W., Mundy, L. G., Kwon, W., & Hamidouche, M. 2007, ApJ, 659, 1404
Tobin, J. J., Hartmann, L., Looney, L. W., & Chiang, H.-F. 2010, ApJ, 712, 1010
Tobin, J. J., Hartmann, L., Chiang, H.-F., et al. 2011, ApJ, 740, 45
Tobin, J. J., Hartmann, L., Chiang, H.-F., et al. 2012, Nature, 492, 83
Tobin, J. J., Dunham, M. M., Looney, L. W., et al. 2015, ApJ, 798, 61
Tobin, J. J., Kratter, K. M., Persson, M. V., et al. 2016a, Nature, 538, 483
Tobin, J. J., Looney, L. W., Li, Z.-Y., et al. 2016b, ApJ, 818, 73
Tokuda, K., Onishi, T., Saigo, K., et al. 2014, ApJ, 789, L4
Tokuda, K., Onishi, T., Matsumoto, T., et al. 2016, ApJ, 826, 26
Tokuda, K., Onishi, T., Saigo, K., et al. 2017, ApJ, 849, 101
Torres, R. M., Loinard, L., Mioduszewski, A. J., & Rodríguez, L. F. 2009, ApJ, 698, 242
Tsukamoto, Y., Iwasaki, K., Okuzumi, S., Machida, M. N., & Inutsuka, S. 2015, MNRAS, 452, 278
Tsukamoto, Y., Okuzumi, S., Iwasaki, K., Machida, M. N., & Inutsuka, S.-i. 2017, PASJ, 69, 95
Ulrich, R. K. 1976, ApJ, 210, 377
Umemoto, T., Iwata, T., Fukui, Y., et al. 1992, ApJ, 392, L83
Verliat, A., Hennebelle, P., Maury, A. J., & Gaudel, M. 2020, A&A, in press, `https://doi.org/10.1051/0004-6361/201936394`
Viotti, R. 1969, Mem. Soc. Astron. It., 40, 75
Ward-Thompson, D., André, P., Crutcher, R., et al. 2007, in Protostars and Planets V, eds. B. Reipurth, D. Jewitt, & K. Keil (Tucson, AZ: University of Arizona Press), 33
Wiesemeyer, H. 1997, PhD thesis, Institut de Radio Astronomie Millimétrique, France
Wiesemeyer, H., Gusten, R., Cox, P., Zylka, R., & Wright, M. C. H. 1998, ASP Conf. Ser., 132, 189
Wiesemeyer, H., Cox, P., Gusten, R., & Zylka, R. 1999,in The Universe as Seen by ISO, eds. P. Cox & M. Kessler (ESA), 427, 533
Williams, J. P., Lee, C. W., & Myers, P. C. 2006, ApJ, 636, 952
Wolf-Chase, G. A., Barsony, M., & O'Linger, J. 2000, AJ, 120, 1467
Yen, H.-W., Takakuwa, S., & Ohashi, N. 2011, ApJ, 742, 57
Yen, H.-W., Takakuwa, S., Ohashi, N., & Ho, P. T. P. 2013, ApJ, 772, 22
Yen, H.-W., Koch, P. M., Takakuwa, S., et al. 2015a, ApJ, 799, 193
Yen, H.-W., Takakuwa, S., Koch, P. M., et al. 2015b, ApJ, 812, 129
Yen, H.-W., Koch, P. M., Takakuwa, S., et al. 2017, ApJ, 834, 178
Yorke, H. W., & Bodenheimer, P. 1999, ApJ, 525, 330
Zhang, Q., Ho, P. T. P., Wright, M. C. H., & Wilner, D. J. 1995, ApJ, 451, L71
Zucker, C., Speagle, J. S., Schlafly, E. F., et al. 2019, ApJ, 879, 125